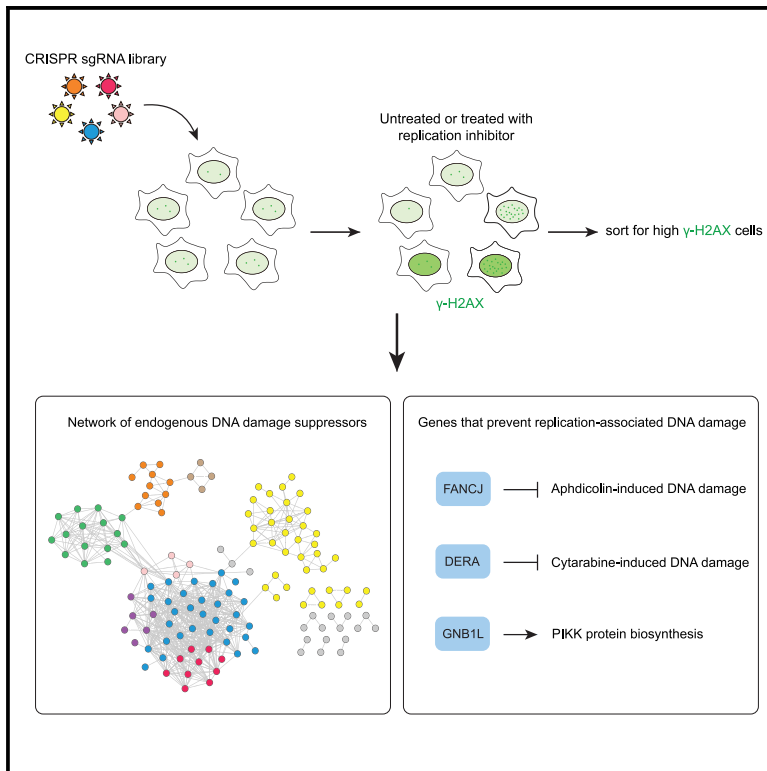


Genome-scale mapping of DNA damage suppressors through phenotypic CRISPR-Cas9 screens

Graphical abstract



Authors

Yichao Zhao, Daniel Tabet, Diana Rubio Contreras, ..., Fernando Gómez Herreros, Frederick P. Roth, Daniel Durocher

Correspondence

durocher@lunenfeld.ca

In brief

Zhao et al. performed phenotypic CRISPR screens to uncover genes and pathways that suppress spontaneous and DNA replication stress-associated DNA damage in human cells. Among the identified genes, *GNB1L*, which is deleted in the 22q11.2 syndrome, is essential for the biosynthesis of kinases of the ATM/ATR family.

Highlights

- Genome-scale phenotypic CRISPR screens identify suppressors of DNA damage
- Genes that suppress spontaneous DNA damage are highly enriched in essential genes
- *DERA* protects cells from cytarabine-induced DNA damage
- *GNB1L* promotes PIKK protein biosynthesis and suppresses replication catastrophe



Resource

Genome-scale mapping of DNA damage suppressors through phenotypic CRISPR-Cas9 screens

Yichao Zhao,^{1,2} Daniel Tabet,^{1,2} Diana Rubio Contreras,³ Linjiang Lao,¹ Arne Nedergaard Kousholt,⁴ Jochen Weile,^{1,2,5} Henrique Melo,¹ Lisa Hoeg,¹ Sumin Feng,¹ Atina G. Coté,¹ Zhen-Yuan Lin,¹ Dheva Setiাপutra,¹ Jos Jonkers,⁴ Anne-Claude Gingras,^{1,2} Fernando Gómez Herreros,³ Frederick P. Roth,^{1,2,5} and Daniel Durocher^{1,2,6,*}

¹Lunenfeld-Tanenbaum Research Institute, Mount Sinai Hospital, 600 University Avenue, Toronto, ON M5G 1X5, Canada

²Department of Molecular Genetics, University of Toronto, 1 King's College Circle, Toronto, ON M5S 1A8, Canada

³Instituto de Biomedicina de Sevilla (IBiS), Manuel Siurot s/n, 41013 Sevilla, Spain

⁴Division of Molecular Pathology, Oncode Institute, The Netherlands Cancer Institute, 1066CX Amsterdam, the Netherlands

⁵Donnelly Centre and Department of Computer Science, University of Toronto, 160 College Street, Toronto M5S 3E1, Canada

⁶Lead contact

*Correspondence: durocher@lunenfeld.ca

<https://doi.org/10.1016/j.molcel.2023.06.025>

SUMMARY

To maintain genome integrity, cells must accurately duplicate their genome and repair DNA lesions when they occur. To uncover genes that suppress DNA damage in human cells, we undertook flow-cytometry-based CRISPR-Cas9 screens that monitored DNA damage. We identified 160 genes whose mutation caused spontaneous DNA damage, a list enriched in essential genes, highlighting the importance of genomic integrity for cellular fitness. We also identified 227 genes whose mutation caused DNA damage in replication-perturbed cells. Among the genes characterized, we discovered that deoxyribose-phosphate aldolase DERA suppresses DNA damage caused by cytarabine (Ara-C) and that *GNB1L*, a gene implicated in 22q11.2 syndrome, promotes biogenesis of ATR and related phosphatidylinositol 3-kinase-related kinases (PIKKs). These results implicate defective PIKK biogenesis as a cause of some phenotypes associated with 22q11.2 syndrome. The phenotypic mapping of genes that suppress DNA damage therefore provides a rich resource to probe the cellular pathways that influence genome maintenance.

INTRODUCTION

To minimize the impact of DNA replication perturbations on the stability of the genome, cells have systems that ensure a robust replication process. For example, stretches of single-stranded DNA (ssDNA) produced following uncoupling of the replicative helicase and DNA polymerases can be sensed by the kinase ataxia telangiectasia and Rad3-related (ATR), which mediates cellular responses to replication stress through the phosphorylation of proteins that include CHK1, RPA, histone H2AX, and SMARCAL1.^{1–4} ATR is recruited to ssDNA via the ATR-interacting protein (ATRIP) and is activated through TOPBP1- or ETAA1-dependent pathways.^{5–7} ATR counteracts replication stress at multiple levels, including stabilizing replication forks, regulating DNA replication origin firing, ensuring deoxyribonucleotide triphosphate (dNTP) availability, and mediating cell cycle checkpoint signaling.⁸

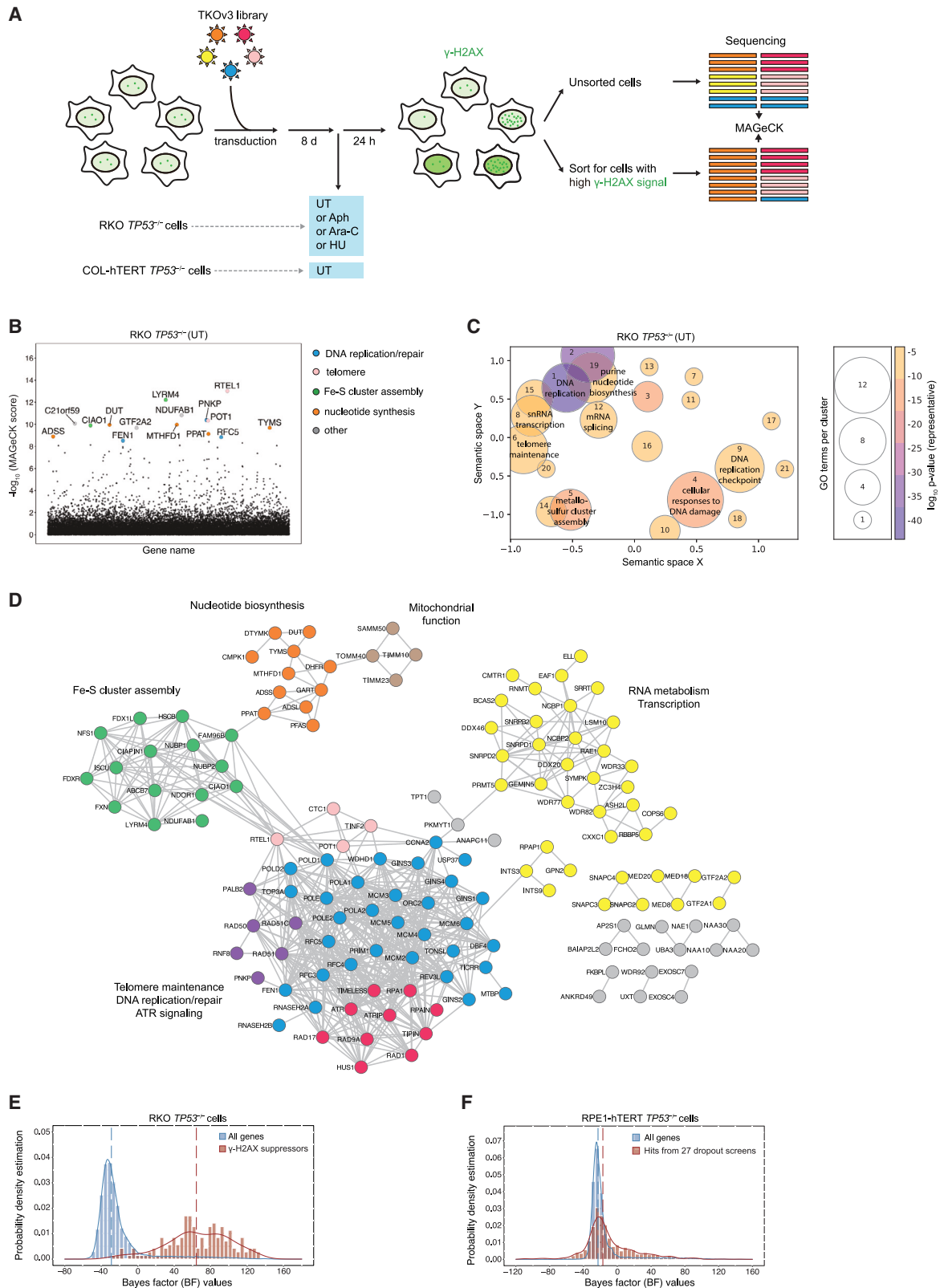
ATR belongs to the family of phosphatidylinositol 3-kinase-related kinases (PIKKs). In mammalian cells, PIKKs have diverse functions in the biology of the DNA damage response (ATR, ATM, and DNA-PKcs), cellular metabolism and proliferation (mTOR), nonsense-mediated mRNA decay (SMG1), and tran-

scription control (TRRAP).^{9,10} PIKKs are large proteins with HEAT repeat-containing N termini followed by C-terminal kinase domains. The protein stability of PIKKs depends on the chaperone HSP90 and the TLO2-TTI1-TTI2 (TTT) co-chaperone complex.^{11–14} The biogenesis of PIKK complexes is known to be essential for genome stability maintenance.¹⁵

We previously undertook the chemogenomic profiling of 27 genotoxic agents using CRISPR-Cas9 genetic screens to identify uncharacterized genome maintenance factors.¹⁶ The resulting dataset identified DNA repair factors and new drug mechanisms of action, but we noted an under-representation of essential genes in the dataset. For example, the gene *RAD51*, which encodes the essential DNA recombinase, was not identified in these screens, most likely because the scoring scheme required single-guide (sg) RNA representation in the control (untreated [UT]) population. Given that genome stability is an essential cellular process, it is likely that other cell-essential genes with roles in genome maintenance were also missed.

To address this shortcoming, we surmised that a screen performed shortly after gene inactivation and using a readout that relies on a DNA damage-linked phenotype would allow the capture of essential genes. We established a phenotypic





(legend on next page)

CRISPR-Cas9 screen pipeline that monitors the level of DNA damage and performed screens in two colon epithelial cell lines, either in the absence of treatment or in the presence of the following replication perturbing agents: aphidicolin (Aph), an inhibitor of B family DNA polymerases¹⁷; hydroxyurea (HU), an inhibitor of ribonucleotide reductase that causes depletion of the cellular dNTP pool¹⁸; and cytarabine (Ara-C), a nucleoside analog that inhibits ribonucleotide reductase activity and blocks DNA replication elongation.¹⁹ These screens revealed insights into the processes that protect cells from DNA damage and identified a number of genes not previously linked to genome maintenance. In particular, we found that the schizophrenia/autism candidate gene *GNB1L* protects cells from replication catastrophe under mild replication perturbation.^{20–22} We uncovered that *GNB1L* promotes the biogenesis of ATR, ATM, and other related PIKKs in collaboration with the TTT complex. The dataset generated in this study therefore offers insights into the processes that prevent the induction of DNA damage under unchallenged conditions as well as under DNA replication stress.

RESULTS

Phenotypic CRISPR-Cas9 screens based on γ -H2AX levels

To probe the processes that prevent the formation of DNA damage independently of their impact on cellular fitness, we established a CRISPR-Cas9 screening strategy based on detecting γ -H2AX by flow cytometry²³ (Figure 1A). The serine 139 residue of histone variant H2AX is quickly phosphorylated in response to DNA lesions and replication blockage, making it a useful marker of DNA damage.²⁴

We carried out CRISPR-Cas9 screens in the RKO colon carcinoma cell line and an hTERT-immortalized, colon epithelial cell line, referred to here as COL-hTERT. The *TP53* gene was knocked out in both cell lines to prevent the potential confounding effects of p53 activation by genotoxic stress. The cell lines are hereafter referred to as RKO *TP53*^{-/-} and COL-hTERT *TP53*^{-/-} (Figure 1A). We carried out 4 screens in the RKO *TP53*^{-/-} cell line: one screen where cells were left UT and one screen each in which cells were treated with low doses of Aph, HU, and Ara-C. The COL-hTERT *TP53*^{-/-} cell line was only screened in the UT condition. The screens were carried with the TKOv3 sgRNA library,²⁵ and cells with the highest 5% of γ -H2AX fluorescence intensity were sorted. Following sgRNA cassette sequencing, gene-level enrichment scores were computed using MAGeCK comparing sgRNA abundance in the

sorted population with that of unsorted cells²⁶ (Figures 1A, 1B, S1A, and S2; Table S1).

Suppressors of γ -H2AX in RKO *TP53*^{-/-} cells

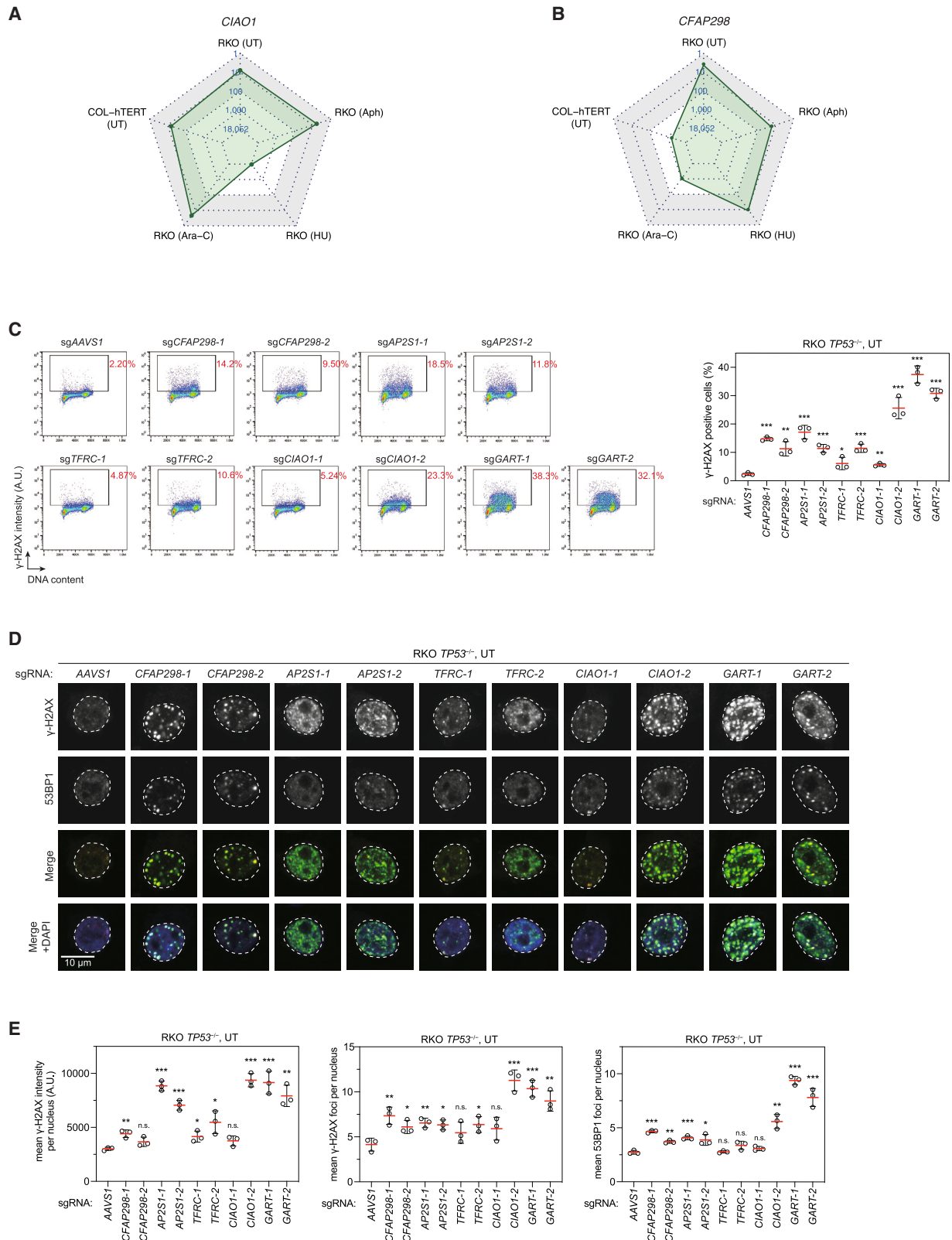
We identified 160 genes whose mutation caused spontaneous high γ -H2AX levels in RKO *TP53*^{-/-} cells (Table S2). This number was obtained by combining 142 genes that scored in the UT screen with a false discovery rate (FDR) value <0.05 along with any other gene with FDR values between 0.05 and 0.1 that were also a hit in the drug-treated screens. Gene ontology (GO) analysis of these hits revealed a strong enrichment for the terms associated with DNA replication (such as GO:0006260), DNA repair (GO:0006281), iron-sulfur (Fe-S) cluster metabolism (GO:0016226), DNA damage signaling (GO:0000076), telomere maintenance (GO:0000723), nucleotide metabolism (GO:0009165), and transcription or splicing (GO:0006366; Figure 1C; Table S3). Most of these biological processes are known to promote genome stability, confirming the ability of γ -H2AX screens to probe pathways involved in genome maintenance.

Gene-level analysis using STRING²⁷ mapped 138 of 160 genes into a network characterized by 4 connected subnetworks enriched in distinct biological processes (Figure 1D). Manual curation of the network nodes revealed a major and dense subcluster of genes with roles in DNA replication, DNA repair, telomere maintenance, and ATR signaling. We also identified subclusters of genes that are involved in nucleotide biosynthesis, RNA metabolism, and transcription, as well as Fe-S cluster assembly (Figure 1D).

Inspection of the gene list revealed the presence of many essential genes, such as those encoding components of the replicative CMG helicase (GINS1–4 and MCM2–6) and replisome proteins (POLA1, POLD1, POLE, PRIM1, etc.). This observation suggested that the γ -H2AX screens succeeded in identifying essential genes. To explore this possibility further, we plotted the Bayes factor (BF) values of the 160 genes and compared them with the BF value distribution of all genes included in the TKOv3 library. BF values represent the likelihood of gene essentiality, with positive BF values indicating probable essential genes.²⁸ The distribution of the 160 genes is remarkably shifted to large positive BF values (median value: 64) compared with the median of all genes (–29; Figure 1E). This is consistent with the notion that genes required to prevent endogenous DNA damage are essential for cell survival. In contrast, analysis of gene hits from our previous fitness-based chemogenomic screens¹⁶ showed both a distribution and a median BF value similar to that of the library (Figure 1F). These results indicate that the phenotype-based γ -H2AX screens did probe the contribution of essential genes to genome maintenance.

Figure 1. Phenotypic CRISPR screens for genes that suppress DNA damage

- (A) Schematic of the phenotypic CRISPR screens based on γ -H2AX staining and cell sorting.
 (B) Manhattan dot plots of γ -H2AX screen results in untreated (UT) RKO *TP53*^{-/-} cells. The top 15 genes are highlighted.
 (C) Gene ontology (GO) analysis of biological process for 160 γ -H2AX suppressors in RKO *TP53*^{-/-} cells, visualized by GO-Figure!
 (D) STRING network analysis of 138 γ -H2AX suppressors in RKO *TP53*^{-/-} cells. Pathways were manually curated and labeled with different colors: green, Fe-S cluster assembly; orange, nucleotide biosynthesis; brown, mitochondrial function; yellow, RNA metabolism and transcription; pink, telomere maintenance; purple, DNA repair; blue, DNA replication; red, ATR signaling; gray, others.
 (E) Distributions of gene essentiality scores (BF values) of γ -H2AX suppressors (brown) and whole genome reference (blue) in RKO *TP53*^{-/-} cells. Kernel density estimation is used for the probability density function. Dashed lines indicate the median for each population.
 (F) Distributions of gene essentiality scores of hits from 27 dropout genotoxic screens (brown) and whole genome reference (blue) in RPE-hTERT *TP53*^{-/-} cells.



(legend on next page)

Suppressors of γ -H2AX in COL-hTERT *TP53*^{-/-} cells

Analysis of the single screen undertaken in COL-hTERT *TP53*^{-/-} cells identified 95 genes whose mutation causes elevated γ -H2AX levels (at FDR < 0.25; Table S2). We employed a more relaxed FDR threshold for this screen because of a lower number of replicates undertaken. GO analysis and network-based representation using STRING showed a similar set of pathways involved in preventing spontaneous γ -H2AX, including DNA replication and Fe-S cluster assembly (Figures S1B and S1C; Table S3). Interestingly, this analysis also identified a unique cluster of genes involved in mitochondrial respiration (such as GO:0042775), suggesting that this pathway contributes to genome stability in this cell line. Similarly, analysis of BF value distribution indicated that suppressors of spontaneous γ -H2AX formation in COL-hTERT *TP53*^{-/-} cells are also enriched in essential genes (Figure S1D).

A total of 32 genes increased γ -H2AX levels in both cell lines when disrupted (Figure S1E). Using a hypergeometric distribution, the probability of having 32 genes co-occurring by chance alone is 1×10^{-42} . Among such genes are those encoding the PRMT5-WDR77 complex, a cancer drug target,²⁹ and multiple genes coding proteins involved in nucleotide metabolism and Fe-S cluster assembly. Together, these results suggest that there are both universal and cell-type-restricted genes that prevent spontaneous DNA damage formation, similar to what has been observed with gene essentiality.³⁰

Validation of genes that prevent endogenous DNA damage

To visualize results at the gene level, we employed radar plots where gene ranking is plotted across the 5 screens. For example, disruption of *CIAO1*, which encodes a protein involved in Fe-S cluster incorporation,³¹ caused high levels of γ -H2AX in 4 of the 5 screen conditions, and disruption of *CFAP298* led to high γ -H2AX levels in 3 of the 4 screens performed in RKO *TP53*^{-/-} but not in COL-hTERT *TP53*^{-/-} cells (Figures 2A and 2B). *CFAP298* is an example of a gene not previously linked to genome maintenance. Mutations in *CFAP298* cause primary ciliary dyskinesia, implicating its product in motile cilium function by acting on the outer dynein arm assembly.³²

To validate the results obtained in unchallenged RKO *TP53*^{-/-} cells, we selected 5 genes whose mutation increases γ -H2AX levels: the aforementioned *CIAO1* and *CFAP298* genes (Figures 2A and 2B), the gene encoding the AP-2 complex component AP2S1, and the gene coding for the transferrin receptor TFRC

involved in iron uptake and *GART*, which codes for an enzyme involved in *de novo* purine biosynthesis (Figure S3). Using independent sgRNAs, we observed that disruption of all five genes caused a higher γ -H2AX signal compared with the AAVS1-targeting sgRNA control, confirming the screen results (Figure 2C). Examination of the γ -H2AX subnuclear localization using immunofluorescence microscopy revealed varied staining patterns for γ -H2AX and 53BP1, a marker of DNA double-strand breaks (DSBs; Figures 2D and 2E). These results suggest that these genes impact genome maintenance via distinct mechanisms. For example, disruption of *CFAP298* caused mainly γ -H2AX and 53BP1 subnuclear foci, which are indicative of DSBs. In contrast, sgRNAs targeting *AP2S1* and *TFRC* induced a pan-nuclear γ -H2AX signal with little increase in foci, suggesting DNA replication stress rather than DSBs. Depletion of *CIAO1* and *GART* produced both pan-nuclear and focal staining of γ -H2AX, suggesting that these genes guard against replication stress and DSB formation.

Validation of genes that prevent replication-associated DNA damage

To identify genes that protect cells against replication stress-induced DNA damage, we searched for genes that increased γ -H2AX levels specifically under conditions when cells were treated with DNA replication inhibitors. This analysis identified 227 genes (Table S2), and we subjected the following genes to validation using independent sgRNAs: *PGD*, which encodes the enzyme 6-phosphogluconate dehydrogenase, the third enzyme in the oxidative pentose phosphate pathway that converts 6-phosphogluconate to ribulose 5-phosphate and produces NADPH³³ (Figure 3A); *DDX5*, encoding an RNA helicase involved in splicing and transcription regulation^{34,35} (Figure 3B); *DDX46*, coding for an RNA helicase that is essential for spliceosome assembly and proofreading of the branch site³⁶ (Figure 3C); *ZNHIT1*, which promotes histone H2A.Z chromatin incorporation to regulate gene expression via its role with the SRCAP complex^{37,38} (Figure 3D); *BRAP*, which encodes a regulator of Ras signaling and cell cycle control^{39,40} (Figure S3K); and *GAS6*, coding for a ligand of TAM receptors⁴¹ (Figure S3L). Four of the six genes tested (*PGD*, *DDX5*, *DDX46*, and *ZNHIT1*) showed replication stress-dependent induction of γ -H2AX, with loss of *DDX5* causing a remarkably selective increase in γ -H2AX following Ara-C treatment (Figure 3B). As *DDX5* resolves R-loops,⁴² one possibility is that *DDX5*-dependent R-loop resolution protects cells from Ara-C-induced DNA damage.

Figure 2. Characterization of genes that prevent spontaneous DNA damage

(A) Radar plot showing the ranking of *CIAO1* in the five γ -H2AX screens. Custom scaling was used for five rings: 1, 10, 100, 1,000, 18,052, and linear scaling was used within each section. The gray-shaded area indicates the top 100 ranking in each screen.

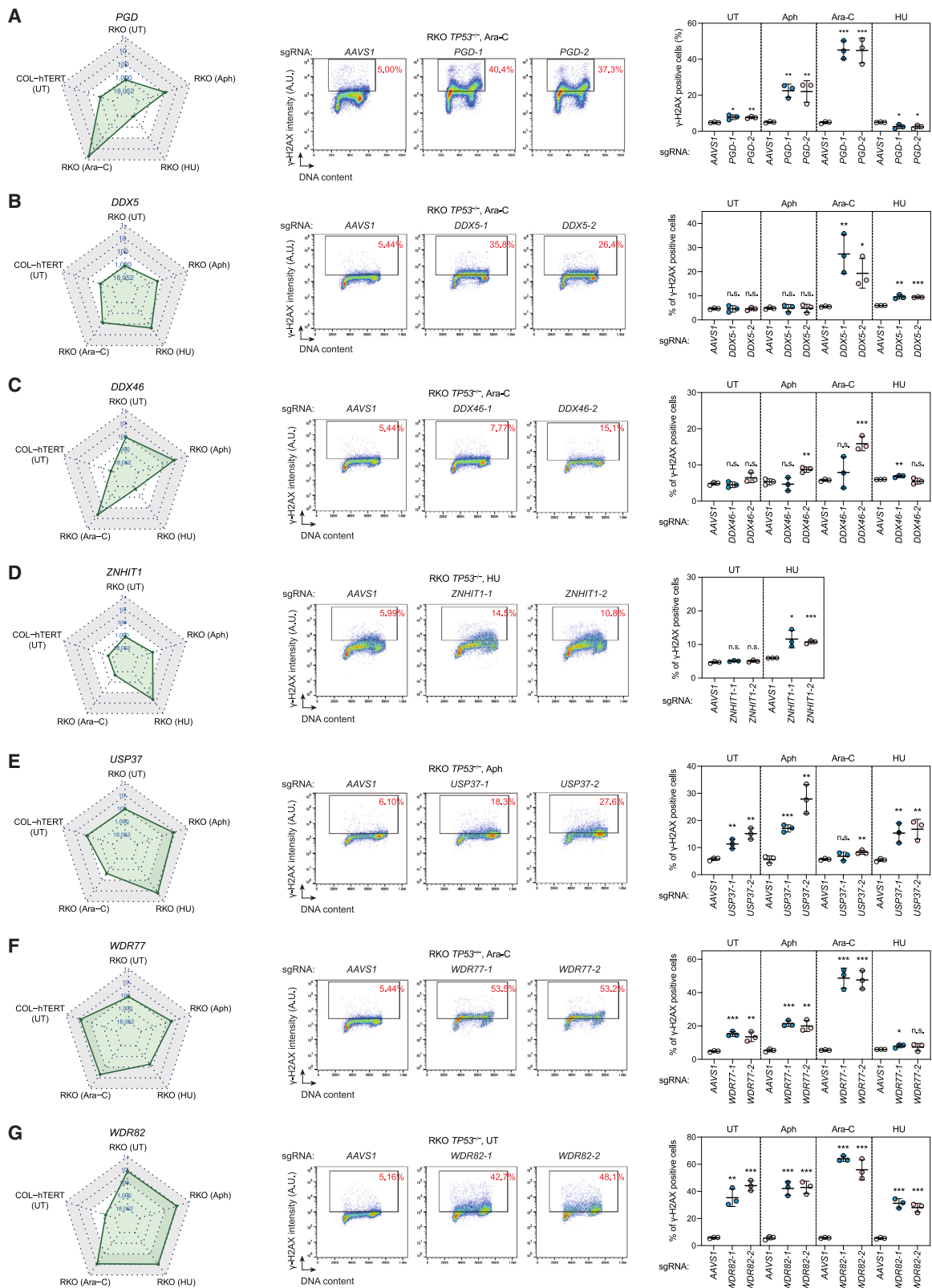
(B) Radar plot showing the ranking of *CFAP298* in five screens.

(C) Flow cytometry analysis of RKO *TP53*^{-/-} cells infected with lentiviruses expressing the indicated sgRNA. Left, representative plots. Red numbers indicate the percentage of γ -H2AX-positive cells. Right, quantification of the experiment shown on the left. Bars represent the mean \pm SD (n = 3). Comparisons are made to the sgAAVS1 control, using an unpaired t test.

(D) Immunofluorescence analysis of cells described in (C) with γ -H2AX and 53BP1 antibodies. The images presented are representative of three immunostainings. Dashed lines indicate the nuclear area determined by 4,6-diamidino-2-phenylindole (DAPI) staining. The scale bar represents 10 μ m.

(E) Quantification of mean γ -H2AX intensity (left), mean γ -H2AX focus number (middle), and mean 53BP1 focus number (right) of three independent experiments as shown in (D). Each experiment includes a minimum of 500 cells for analysis. Bars represent the mean \pm SD. Comparisons were made to the sgAAVS1 condition using an unpaired t test. a.u., arbitrary units.

*p < 0.05, **p < 0.01, ***p < 0.001. ns, not significant.



(legend on next page)

We also validated three genes that prevent high γ -H2AX levels in both the UT condition and conditions with replication stressing agents: *USP37*, which encodes a deubiquitinase possibly involved during DNA replication^{43,44} (Figure 3E); *WDR77*, coding for a component of the PRMT5-WDR77 methylosome⁴⁵ (Figure 3F); and *WDR82*, which encodes a member of the SET1 methyltransferase complex⁴⁶ (Figure 3G). Together, this validation effort suggests that the γ -H2AX screen dataset can be mined for genes and pathways that promote genome integrity. Below, we highlight a few genes identified in the screens, along with a deeper characterization of *GNB1L*.

FANCD1 protects cells from Aph-induced replication stress

FANCD1 (also known as *BACH1* or *BRIP1*) was a top-ranking gene in the Aph γ -H2AX screen (Figure 4A). *FANCD1* is a well-characterized DNA helicase first identified as a BRCA1-interacting protein.⁴⁷ We confirmed that cells expressing *FANCD1*-targeting sgRNAs display a large increase in γ -H2AX following Aph treatment, with a comparatively smaller increase following Ara-C treatment (Figure 4A). Interestingly, a parallel CRISPR-Cas9 fitness screen in RKO *TP53*^{-/-} cells identified sgRNAs targeting *FANCD1* as the top sensitizer to a low-dose Aph treatment (Figure S4A), indicating that *FANCD1* plays a key role in mitigating the impact of DNA polymerase inhibition in human cells.

We next generated CRISPR knockout (KO) clones of *FANCD1* in RKO *TP53*^{-/-} cells (Figure 4B) that were hypersensitive to Aph, as expected (Figure 4C). Under Aph challenge, *FANCD1*-KO cells accumulate in the S phase (Figure S4B) and show a striking increase in pan-nuclear γ -H2AX staining accompanied by a concomitant increase in chromatin-bound RPA2, which is part of the ssDNA-binding complex RPA (Figure 4D). These results suggest that *FANCD1* loss causes widespread replication perturbation characterized by the generation of ssDNA.

The formation of ssDNA in *FANCD1*-KO cells following a 24 h Aph treatment was accompanied by increased ATR signaling, as monitored through CHK1-S345 and RPA2-S33 phosphorylation (Figure 4E) that gradually decreased to reach baseline levels 8 h post-Aph washout. Similarly, the striking S-phase accumulation of *FANCD1*-KO cells in the presence of low-dose Aph was resolved within 8 h, with cell cycle profiles becoming undistinguishable from parental cells (Figure 4F). These observations suggest that the DNA lesions in *FANCD1*-KO cells are largely reversible, although some lesions must persist to cause the hypersensitivity of *FANCD1*-KO cells to Aph treatment.

The ssDNA accumulation in *FANCD1*-KO cells under Aph treatment could be either in the form of ssDNA gaps or long ssDNA tracts. To discriminate between these possibilities, we per-

formed DNA fiber experiments with or without S1 nuclease, which converts ssDNA gaps to DSBs⁴⁸ (Figures 4G and 4H). In the absence of S1 nuclease, *FANCD1*-KO cells had shorter 5-iodo-2'-deoxyuridine (IdU) tracts than wild-type (WT) cells under Aph treatment, consistent with a slower proliferation rate (Figure 4C). The S1 nuclease treatment led to shorter IdU tracts in the parental cells, indicating the presence of ssDNA gaps. However, the S1 nuclease did not further shorten IdU tracts in *FANCD1*-KO cells, suggesting either that the ssDNA gaps were generated in a *FANCD1*-dependent manner, as in Peng et al.⁴⁹ and Cong et al.⁵⁰ or that ssDNA in *FANCD1*-KO cells was in the form of longer ssDNA tracts (Figures 4G–4I).

In budding yeast, ssDNA is repaired following recruitment of translesion synthesis (TLS) polymerases⁵¹ in a PCNA ubiquitylation-dependent manner.⁵² We monitored monoubiquitylation of PCNA Lys164 after Aph treatment and release and observed that *FANCD1*-KO cells displayed a transient increase in PCNA ubiquitylation that peaked 1 h post-release (Figure 4E). These observations suggest that under Aph challenge, *FANCD1*-deficient cells accumulate ssDNA tracts that may be reversed in part by the action of TLS polymerases.

The γ -H2AX accumulation displayed by *FANCD1*-KO cells during Aph treatment is rescued by lentiviral expression of WT *FANCD1* (Figures S4C–S4E). This allowed us to functionally profile the following *FANCD1* mutants: K52R, which disrupts helicase activity⁴⁷; K141A/K142A, which impairs interaction with MLH1⁵³; S990A, which abolishes interaction with BRCA1⁵⁴; and T1133A, which blocks binding to TOPBP1.⁵⁵ Reintroduction of these mutants, with the notable exception of *FANCD1*-K52R, completely suppressed γ -H2AX accumulation in the presence of Aph (Figures S4C–S4E). Identical results were obtained in hTERT-immortalized retinal pigment epithelium-1 (RPE1) cells where the *FANCD1* mutations were introduced at the chromosomal locus via gene editing (Figure S4F; Table S4). These results suggest that the *FANCD1* helicase activity, but not its role in DNA interstrand crosslink (ICL) repair, homologous recombination (HR), or DNA damage signaling, is essential to protect cells from DNA replication stress. We surmise that under conditions of perturbed replication, such as under Aph challenge, *FANCD1* resolves DNA obstacles with its helicase activity, thereby allowing DNA synthesis to bypass the obstacle and generating the ssDNA gap that can be repaired later (Figure 4I).

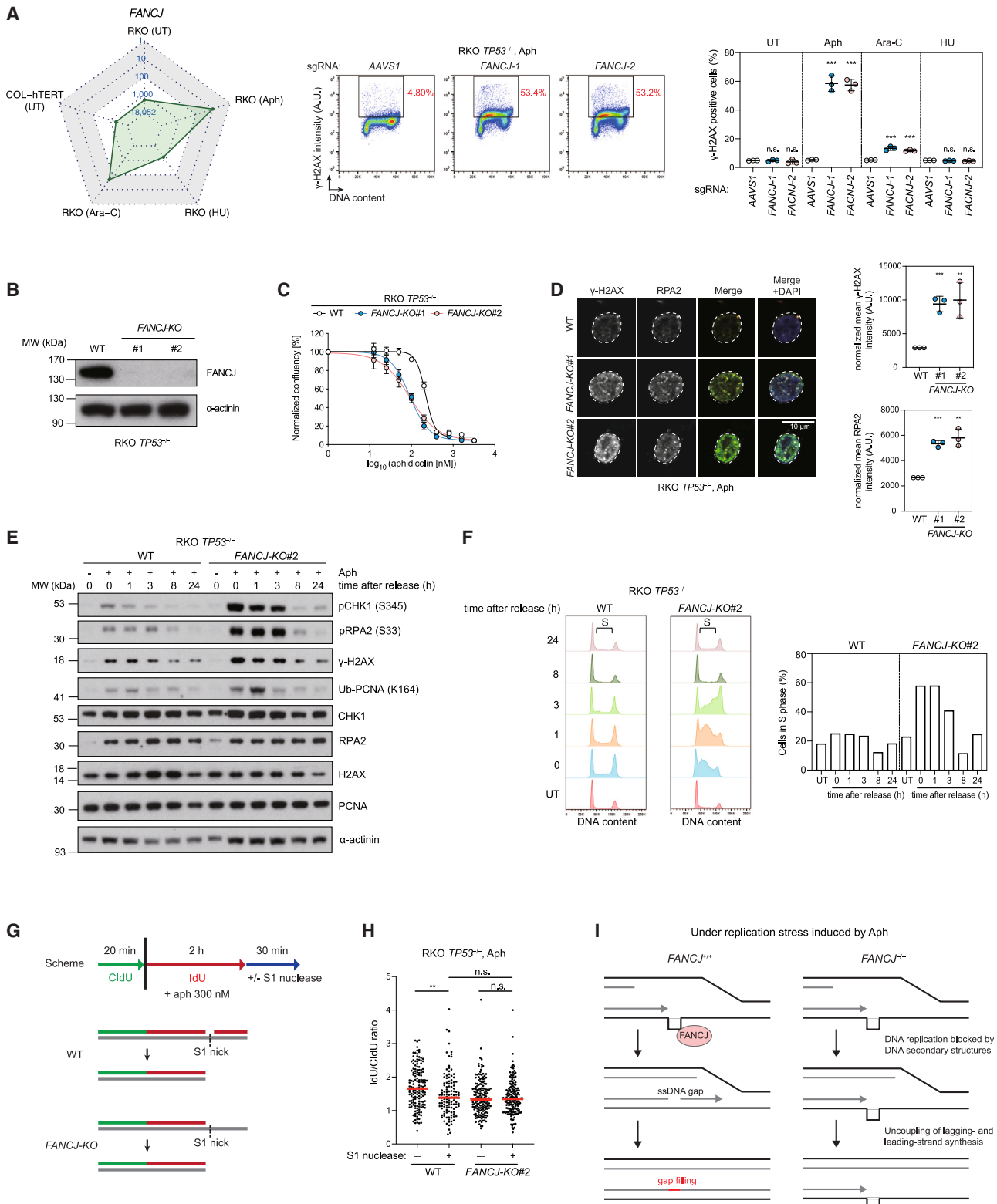
DERA protects cells from Ara-C

DERA was a top-ranking gene in the Ara-C γ -H2AX screen, which we validated with independent sgRNAs (Figure 5A). *DERA* is a deoxyribose-phosphate aldolase, which participates in nucleotide catabolism and the pentose phosphate pathway.⁵⁶ *DERA* is specifically required to prevent DNA damage induced by Ara-C but not by Aph or HU (Figure 5A), and *DERA*-targeting

Figure 3. Validation of genes that suppress replication-associated DNA damage

(A–G) Validation of the screens. Left, the radar plot showing the ranking of each gene in five screens. Middle, representative flow cytometry plots of RKO *TP53*^{-/-} cells expressing the indicated sgRNA. Cells were treated with the indicated replication inhibitor for 24 h or left untreated (UT). 300 nM Aph, 200 nM Ara-C, and 200 μ M HU were used in this experiment, and the same drug concentrations were used for subsequent experiments unless otherwise specified. Right, quantification of γ -H2AX positive cells in all conditions. Bars represent the mean \pm SD ($n = 3$). Comparisons are made to the sgAAVS1 control within each treatment condition using an unpaired t test. The Ara-C experiments in (B), (C), and (F) were performed simultaneously with the same sgAAVS1 control.

* $p < 0.05$, ** $p < 0.01$, *** $p < 0.001$. ns, not significant.



(legend on next page)

sgRNAs impair cell proliferation in the presence of low-dose Ara-C but not in UT cells (Figure 5B). Introduction of WT DERA in *DERA*-depleted cells, but not a catalytic-dead (K254A) variant, restored normal γ -H2AX levels following Ara-C treatment, suggesting that the aldolase activity of DERA prevents DNA damage formation (Figures 5C and 5D). We also assessed γ -H2AX formation in response to two other related nucleoside analogs, gemcitabine or fludarabine (Figures 5E and 5F). Ara-C and fludarabine share an arabinose backbone but differ by the nitrogenous base, whereas gemcitabine and Ara-C share the cytosine base but differ in their sugar moieties (Figure 5E). We found that *DERA*-deficient cells display higher γ -H2AX levels following treatment with fludarabine but not gemcitabine (Figure 5F), suggesting that DERA specifically protects cells from arabinoside analogs. Although we have not determined the exact mechanism of action of DERA on Ara-C, we anticipate that it may relate to the action of DERA on a Ara-C metabolite, possibly 5-deoxyarabinose-phosphate.⁵⁶

RECQL5 protects cells from replication-associated DSBs

RECQL5 is representative of a gene whose mutation increased γ -H2AX levels under the three types of DNA replication stress tested (Figure S5A). *RECQL5* encodes a RecQ-type 3'-5' DNA helicase implicated in DNA repair and replication.⁵⁷ Independent sgRNAs targeting *RECQL5* caused increased γ -H2AX in response to Aph, HU, or Ara-C compared with controls, confirming the screen results (Figure S5A). *RECQL5*-deficient cells accumulated γ -H2AX and 53BP1 foci following Aph treatment, suggesting the formation of DSBs (Figure S5B). A clonal KO of *RECQL5* also showed elevated γ -H2AX levels following Aph treatment, a phenotype that we could suppress by reintroducing *RECQL5* with lentiviral transduction (Figures S5C and S5D). This system allowed us to test *RECQL5* variants that disrupt either its helicase activity (K58R), its phosphorylation by CDK1 (S727A), or its interaction with RAD51 (F666A) or RNA polymerase II (RNAPII; E584D).^{57–59} To our surprise, every *RECQL5* point mutant complemented *RECQL5*-KO cells to the same extent as WT *RECQL5* (Figures S5C–S5E). To narrow down the *RECQL5* domain involved in suppressing Aph-induced H2AX phosphorylation, we tested a series of *RECQL5* truncation mutants and found that a *RECQL5* C-terminal region (residues 491–991) was both

sufficient and necessary for full suppression of the γ -H2AX phenotype (Figures S5F–S5H). These results suggest that both the internal RNAPII interaction domain (IRI, located between the 491–620 residues) and the SET2-RPB1-interacting domain (SRI, 901–991) participate in the suppression of DSB formation following replication stress (Figure S5E).

GNB1L prevents replication catastrophe under mild replication stress

Disruption of *GNB1L* caused high γ -H2AX levels following treatment with replication inhibitors, with a particularly strong response in the HU screen (Figure 6A). *GNB1L* was of particular interest since it has been repeatedly linked to schizophrenia and autism in genetic association studies.^{20,22,60} *GNB1L* encodes a protein of unknown function consisting of seven predicted WD40 repeats.^{61,62}

RKO *TP53*^{-/-} and RPE1-hTERT *TP53*^{-/-} cells expressing *GNB1L*-targeting sgRNAs display a massive increase in γ -H2AX in S-phase cells, specifically under conditions of mild replication stress (Figures 6B, 6C, and S6A). This γ -H2AX induction was reminiscent of replication catastrophe, a condition caused by extensive ssDNA that triggers exhaustion of the RPA pool, leading to unprotected ssDNA and subsequent DSB formation.⁶³ *GNB1L* loss also greatly potentiated γ -H2AX induction under low doses of CD437, a DNA polymerase α inhibitor⁶⁴ that is particularly efficient at eliciting replication catastrophe⁶⁵ (Figures 6B, 6C, and S6A). Quantitative image-based cytometry (QIBC) monitoring H2AX phosphorylation and the extent of RPA-bound ssDNA indicated that *GNB1L* depletion caused the accumulation of cells with both high γ -H2AX and chromatin-bound RPA signals under mild replication stress (Figures 6D and S6B), a phenotype that could be rescued by inhibiting origin firing with CDK2 or CDC7 inhibitors (PF-06873600 and TAK-931, respectively; Figures S6B and S6C). Together, these results indicate that *GNB1L* guards against DNA replication catastrophe. Consistent with this, *GNB1L*-deficient cells display impaired proliferation in the presence of HU or gemcitabine (Figure S6D).

GNB1L interacts with PIKKs and the TTT complex

To gain insights into the mechanism by which *GNB1L* protects cells under replication stress, we searched for interacting

Figure 4. *FANCI* protects cells from Aph-induced replication stress

(A) Left, radar plot showing the ranking of *FANCI* in the five γ -H2AX screens. Middle, flow cytometry analysis of RKO *TP53*^{-/-} cells expressing the indicated sgRNA. Right, quantification of γ -H2AX positive cells in all four conditions. Bars represent the mean \pm SD (n = 3). Comparisons are made to the sgAAVS1 control within each treatment condition using an unpaired t test.

(B) Immunoblot analysis of *FANCI* expression in RKO *TP53*^{-/-} parental (WT) and *FANCI*-KO cells. α -actinin was used as a loading control.

(C) Aph dose-response assays using confluency as a readout 6 days post-treatment. Bars represent the mean \pm SD (n = 3).

(D) Left, immunofluorescence analysis of γ -H2AX and chromatin-bound RPA2. Right, quantification of normalized mean intensities of γ -H2AX and RPA2. Bars represent the mean \pm SD (n = 3). Results of unpaired t test between WT and *FANCI*-KO cells are shown. a.u., arbitrary units. The scale bar represents 10 μ m.

(E and F) Recovery assay from Aph treatment. Cells were left untreated (-) or treated with 300 nM Aph for 24 h, then released into cell growth medium without the drug for the indicated time before harvesting. (E) Immunoblot analysis using the indicated antibodies. α -actinin, loading control. (F) Cell cycle distributions as determined by DAPI staining. UT, untreated. Brackets indicate S-phase cells.

(G) Schematic of DNA fiber experiments.

(H) Quantification of 5-iodo-2'-deoxyuridine (IdU)/5-chloro-2'-deoxyuridine (CldU) ratio. Each dot represents one fiber; at least 120 fibers are quantified from three independent experiments. Red bars represent the median. Results of the unpaired t test are shown.

(I) Model of *FANCI* at the DNA replication fork.

*p < 0.05, **p < 0.01, ***p < 0.001. ns, not significant.

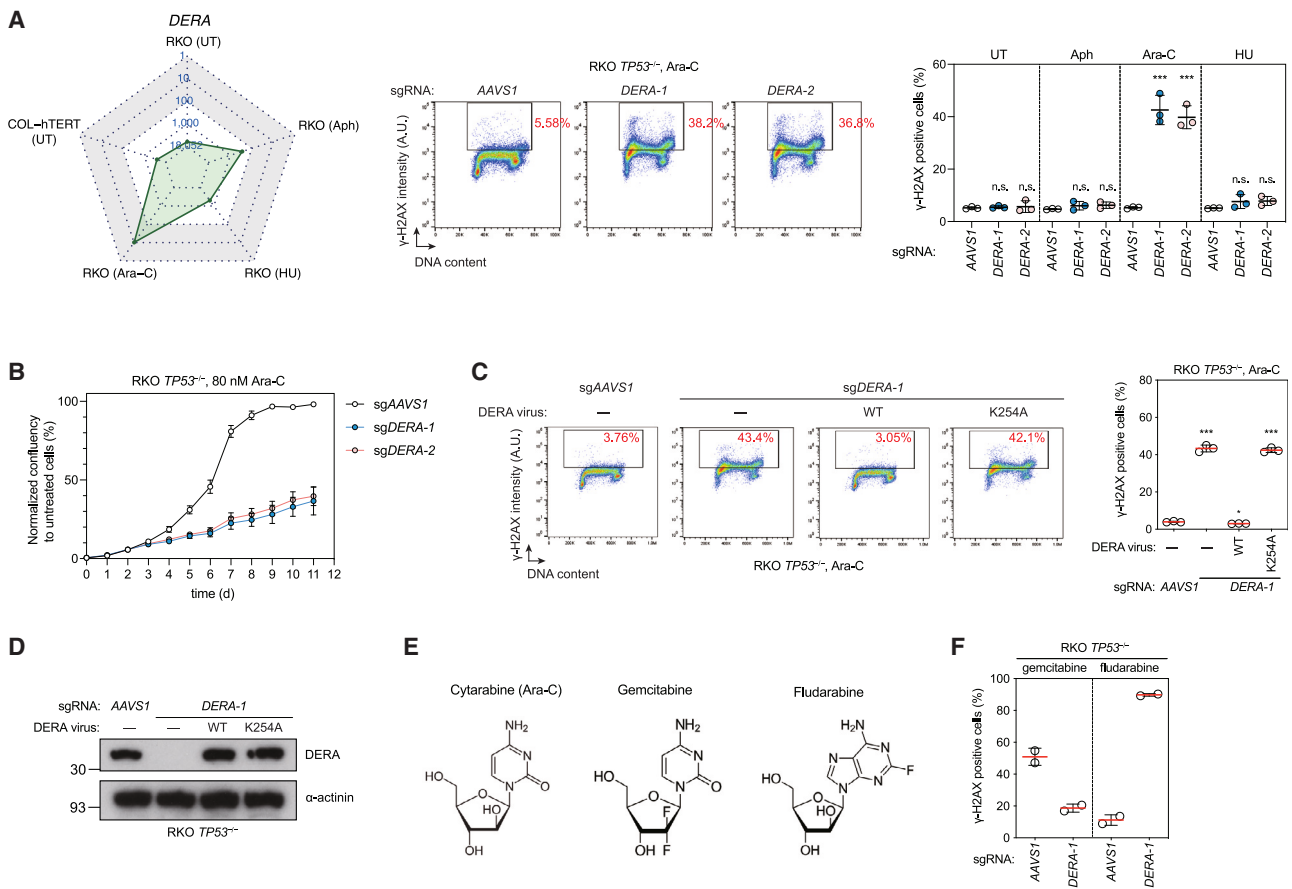


Figure 5. *DERA* protects cells from Ara-C

(A) Left, radar plot showing the ranking of *DERA* in the five γ -H2AX screens. Middle, flow cytometry analysis of RKO *TP53*^{-/-} cells expressing the indicated sgRNA. Right, quantification of γ -H2AX positive cells in all four conditions. Bars represent the mean \pm SD (n = 3). Comparisons are made to the sgAAVS1 control within each treatment condition using an unpaired t test.

(B) Proliferation curves of RKO *TP53*^{-/-} cells expressing sgAAVS1 control or sgDERA in the presence of 80 nM Ara-C. Confluency is normalized to the untreated condition for each genotype. Data are presented as mean \pm SD (n = 3).

(C) Flow cytometry analysis of sgDERA-expressing cells complemented with sgRNA-resistant wild-type (WT) or catalytic-dead (K254A) mutant of *DERA*. Cells were treated with 200 nM Ara-C for 24 h. Left, representative flow cytometry plots. Right, quantification of γ -H2AX positive cells. Bars represent the mean \pm SD (n = 3). Comparisons are made to the sgAAVS1 control using an unpaired t test.

(D) Immunoblot analysis of *DERA* expression in cells described in (C). α -actinin, loading control.

(E) Chemical structures of cytarabine (Ara-C), gemcitabine, and fludarabine.

(F) Flow cytometry analysis of sgAAVS1 or sgDERA-expressing cells treated with 20 nM gemcitabine or 5 μ M fludarabine for 24 h. Bars represent the mean \pm SD (n = 2).

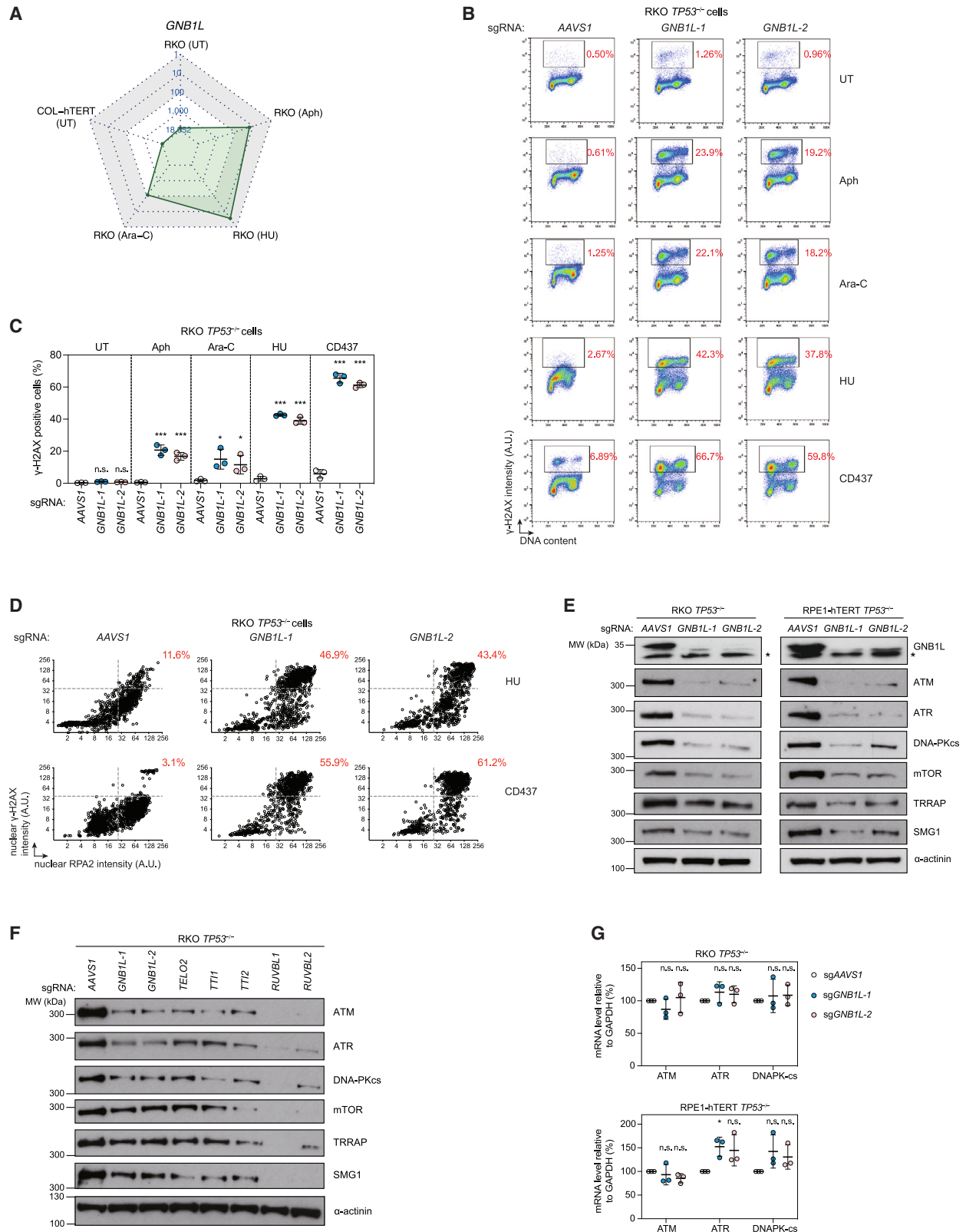
*p < 0.05, **p < 0.01, ***p < 0.001. ns, not significant.

proteins with affinity purification coupled to mass spectrometry (AP-MS) and proximity-based interaction proteomics using the miniTurbo system.⁶⁶ After filtering hits with SAINT,⁶⁷ TELO2 was the only high-confidence protein interacting with GNB1L in the AP-MS experiment (Figure S7A; Table S5). In contrast, proximity interaction proteomics not only retrieved TELO2 but also identified TTT1 and all six members of the PIKK family (DNA-PKcs, ATM, ATR, mTOR, SMG1, and TRRAP; Figure S7A; Table S5). Streptavidin pulldowns followed by immunoblotting in cells expressing miniTurbo-tagged GNB1L (Figure S7B) confirmed that the TTT complex and each PIKK protein reside in the proximity of GNB1L. Similarly, the same proteins, except SMG1, could be retrieved in GNB1L immunoprecipitates,

suggesting more intimate interactions than anticipated from the AP-MS experiment (Figure S7C). Finally, we used the NanoBRET assay⁶⁸ to confirm a physical interaction between GNB1L and TELO2 in cells (Figure S7D).

GNB1L promotes PIKK protein biogenesis

The identification of TTT, RUVBL1/2, and PIKKs as GNB1L-interacting proteins was revealing because the replication catastrophe seen in GNB1L-deficient cells is a phenocopy of ATR loss or inhibition.⁶³ Given that TTT and RUVBL1/2 promote ATR (and PIKK) biogenesis, these results suggested that GNB1L may also participate in the same process. Indeed, transduction of *GNB1L*-targeting sgRNAs caused a reduction in the



(legend on next page)

steady-state levels of all PIKKs, with the DNA damage-related factors, ATM, ATR, and DNA-PKcs, being the most affected (Figure 6E). The reduction in PIKK levels was similar to that observed in cells depleted of TTT complex members (Figures 6F and S7E), which also caused a replication catastrophe-like phenotype under replication stress (Figure S7F). The reduced PIKK levels in GNB1L-depleted cells were not due to reduced mRNA levels, at least for the 3 PIKKs tested (Figure 6G). To assess if the reduction of PIKKs impaired function, we assessed the integrity of ATM, ATR, and mTOR signaling by immunoblotting. Substrate phosphorylation by ATR, ATM, and mTOR was compromised in GNB1L-depleted cells after stimulation (Figure S7G). Together, these results indicate that GNB1L promotes the biogenesis of functional PIKK proteins.

TELO2 stabilizes newly synthesized but not pre-existing PIKKs.¹² To test whether GNB1L promotes the biogenesis of newly synthesized PIKKs, we first generated a cell line in which the GNB1L protein can be rapidly depleted using the dTAG system^{69,70} (Figure S8A). Over time, GNB1L depletion caused a reduction in the protein levels of ATM, ATR, and DNA-PKcs and sensitized cells to replication catastrophe (Figures S8A and S8B). To monitor ATR biogenesis, we expressed Halo-tagged ATR, which enabled us to follow the abundance of newly synthesized or pre-existing ATR using label-switch strategies (Figures S8C and S8D). We found that GNB1L depletion selectively impacted the accumulation of newly synthesized ATR (Figures S8C and S8D). We conclude that GNB1L, like TELO2, promotes the biogenesis of newly synthesized PIKKs, including that of ATR.

Deep mutational scanning of GNB1L

The observation that GNB1L is predicted to form a single WD40 repeat propeller as a folded unit suggested that deletion mutagenesis to identify functionally important regions of GNB1L would be impossible. As an alternative, we applied deep mutational scanning to identify variants of GNB1L that promote replication catastrophe.⁷¹ We constructed a lentiviral GNB1L mutant library of 5,529 mutants in which GNB1L is expressed as a C-terminal GFP fusion (Figure S9A). After library transduction, we sorted for GFP-positive cells to remove variants that caused loss of GNB1L expression. Endogenous GNB1L was then inactivated with a sgRNA. The resulting pool of cells was treated with HU and subsequently sorted for cells with high γ -H2AX (Fig-

ure S9A). Mutant frequency was determined using Tileseq.^{72,73} A “functional” score was assigned to each mutant (Table S6), where mutations enriched in the high γ -H2AX population were assigned low functional scores.

To validate this analysis, we examined the relationship between the median functional score for each GNB1L residue and a corresponding median change in Gibbs free energy ($\Delta\Delta G$) computed with FoldX⁷⁴ (Figure S9B; Table S6). We observed an inverse correlation between functional scores and the median $\Delta\Delta G$ (Pearson correlation -0.61), suggesting that substitutions that perturb folding are functionally impaired, as expected. Similarly, using conservation computed with ConSurf (Figure S9B; Table S6), where negative values indicate conservation, we observed a positive correlation between functional and conservation scores (Pearson correlation 0.58). Together, these analyses indicate that our mutational scanning pipeline is effective at identifying variants that impair GNB1L function.

We next mined this dataset to identify variants with low-to-medium $\Delta\Delta G$ scores (i.e., minimal impact on protein folding) that negatively impact GNB1L function. We selected 6 high-confidence variants for retesting: S42L, G43M, A271E, G272R, D274G, and D315R (Table S6). Reintroduction of each variant failed to rescue HU-induced γ -H2AX levels, indicating that they were all functionally defective (Figures S9C and S9D). Although the expression of these GNB1L variants was lower than that of exogenously expressed GNB1L, they were all expressed at levels higher than endogenous GNB1L in the parental cell line (Figure S9C), displayed lower levels of ATM, ATR, and DNA-PKcs proteins (Figure S9C), and all were impaired in their interaction with TELO2 and ATM (Figure S9E), suggesting that the integrity of the GNB1L-TELO2 complex is critical for PIKK biogenesis. Exactly how these mutations impact GNB1L function is unclear, but as they are not concentrated on any one area of the proteins, we surmise that a subset of them act by subtly destabilizing GNB1L.

GNB1L-TELO2 promotes PIKK levels

In parallel, we mapped the region of TELO2 involved in its interaction with GNB1L. The region of TELO2 that is necessary and sufficient to interact with GNB1L is encompassed by residues 460–545 (Figures 7A, S10A, and S10B), consistent with an AlphaFold2 model of the GNB1L-TELO2 complex that identified

Figure 6. GNB1L protects cells under replication stress and promotes PIKK protein stability

(A) Radar plot showing the ranking of GNB1L in five screens.

(B) Representative flow cytometry analysis of RKO TP53^{-/-} cells expressing the indicated sgRNA. Cells were treated with the indicated replication inhibitor for 24 h or left untreated (UT), then fixed and stained with a γ -H2AX antibody and DAPI.

(C) Quantification of the experiment shown in (B). Bars represent the mean \pm SD (n = 3). Comparisons are made to the sgAAVS1 control within each treatment condition using an unpaired t test.

(D) QIBC analysis of γ -H2AX and chromatin-bound RPA2 signal intensities in RKO TP53^{-/-} cells. Cells were treated with 200 μ M HU or 250 nM CD437 for 24 h, then extracted, fixed, and stained with antibodies to γ -H2AX and RPA2. Red numbers indicate the percentage of cells with high γ -H2AX and high RPA2 signal for each condition. a.u., arbitrary units.

(E) Immunoblot analysis of PIKKs in lysates from RKO TP53^{-/-} and RPE-hTERT TP53^{-/-} cells expressing sgAAVS1 control or sgGNB1L. α -actinin, loading control. Asterisk denotes non-specific bands.

(F) Immunoblot analysis of PIKKs in lysates from RKO TP53^{-/-} cells expressing the indicated sgRNA.

(G) Quantitative reverse transcription (RT)-PCR experiments to detect the mRNA levels of ATM, ATR, and DNA-PKcs using TaqMan assays. Bars represent the mean \pm SD (n = 3). Comparisons are made to the sgAAVS1 control using an unpaired t test.

*p < 0.05, **p < 0.01, ***p < 0.001. ns, not significant.

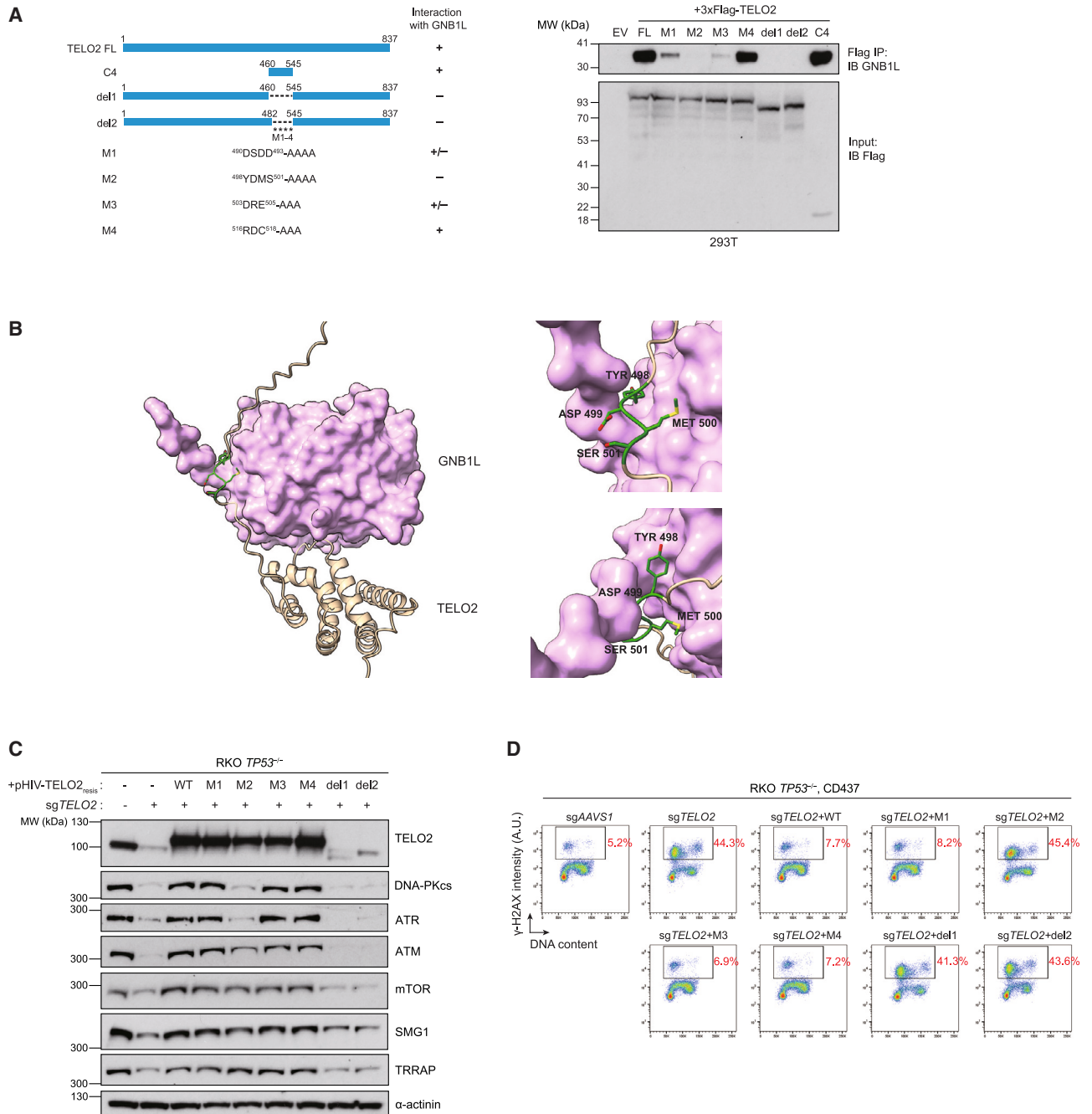


Figure 7. GNB1L-TELO2 interaction promotes PIKK levels

(A) Left, schematic of TELO2 truncations and mutations. Right, FLAG immunoprecipitation in lysates of 293T cells expressing full-length (FL) or mutant 3xFlag-TELO2 and probed for GNB1L.

(B) Left, AlphaFold2-predicted structure of full-length GNB1L binding to a TELO2 fragment (residues 460–640). Purple, surface structure of GNB1L. Beige, ribbon structure of the TELO2 fragment. Right, magnified view of binding surface. Residues 498–501 of TELO2 are labeled and highlighted in green.

(C and D) RKO *TP53*^{-/-} cells were infected with lentiviruses expressing sgTELO2 and sgRNA-resistant TELO2 variant constructs as indicated. WT, wild type. (C) Immunoblot analysis of cell lysates with the indicated antibodies. α -actinin, loading control. (D) Cells were treated with 250 nM CD437 for 24 h, then fixed and stained with a γ -H2AX antibody and DAPI. Red numbers indicate the percentage of γ -H2AX-positive cells. The results are representative of two independent experiments. a.u., arbitrary units.

a TELO2 loop encompassing these residues as directly interacting with GNB1L⁷⁵ (Figures 7B, S10C, and S10D; Table S7). Alanine scanning of this region identified a TELO2 mutant we designated as M2 (⁴⁹⁸YMDS⁵⁰¹-AAAA) that was completely deficient in GNB1L binding, in protecting cells against replication catastrophe, and which displayed impaired PIKK levels (Figures 7C and 7D). This was in contrast to the corresponding single-point mutants, which were impaired in TELO2 binding but displayed both normal PIKK levels and responses to CD437 treatment (Figures S10E–S10G). These results indicate that a minimal TELO2–GNB1L interaction is both sufficient and necessary for PIKK stability and guards against replication catastrophe.

DISCUSSION

This work presents a genome-scale survey of the genes and pathways that protect cells against DNA damage using H2AX phosphorylation as a readout. This dataset can be mined for the identification of genes not previously associated with genome maintenance. For example, we identified *CFAP298*, a gene previously linked to ciliogenesis,³² as suppressing the formation of spontaneous DSBs.

One of the most surprising findings of this study was that the genes suppressing spontaneous DNA damage were functionally enriched in only a handful of biological processes. These include DNA replication, DNA repair, RNA metabolism, and a few biosynthetic pathways such as nucleotide metabolism and Fe-S cluster biogenesis. These results may imply that the genome is insulated from a majority of cellular processes, which would effectively minimize the impact of their dysfunction on the integrity of the genome.

Among the genes that suppress spontaneous γ -H2AX formation in RKO *TP53*^{-/-} cells, 15 encode proteins participating in Fe-S cluster assembly, and three (*AP2S1*, *TFRC*, and *FCHO2*) code for factors involved in iron uptake by endocytosis. This observation further highlights a key role of iron metabolism in genome stability, which can be explained by the fact that many DNA replication and repair proteins require a Fe-S cluster as their cofactor.⁷⁶ Furthermore, although mitochondrial dysfunction is often assumed to cause nuclear DNA damage solely due to oxidative stress,⁷⁷ defective Fe-S cluster assembly may be another important mitochondrial source of nuclear genome damage. This is consistent with work done in yeast that linked genome instability caused by age-related mitochondrial dysfunction to defective Fe-S cluster assembly.⁷⁸ These observations also suggest that modulating iron uptake or Fe-S cluster assembly could be used to induce DNA damage for therapeutic purposes, but such strategies would need to be optimized to avoid an impact on physiological processes that require iron uptake, such as erythropoiesis.

Our structure-function studies indicate that the roles of RECQL5 and FANCI in suppressing replication-associated DNA damage may be distinct from some of their better-described functions. However, as the motor/helicase activity of FANCI was the sole activity necessary to suppress ssDNA accumulation in response to Aph treatment, our results are clearly consistent with the recently described model of FANCI action at forks stalled with DNA-protein cross-links.⁷⁹ FANCI uses its

motor activity in concert with RTEL1 to overcome the barrier to leading-strand replication. Interestingly, RTEL1 drives the formation of an ssDNA substrate by translocating on the undamaged strand, and we predict that in the absence of FANCI, RTEL1 action may result in the long ssDNA tracts we have observed in *FANCI*-KO cells.

Finally, we describe GNB1L as a PIKK biogenesis factor that cooperates with the TTT-RUVBL1/2 co-chaperone complex. In budding yeast, the Tel2-Tti1-Tti2 complex promotes the protein stability of the homologs of ATR and ATM (Mec1 and Tel1, respectively) through an Asa1-dependent pathway.⁸⁰ Asa1 is a WD40 repeat protein with limited homology to GNB1L, but as noted previously,⁸¹ GNB1L likely represents the Asa1 homolog in vertebrates. Since *GNB1L* haploinsufficiency is a candidate gene for the neuropsychiatric disorders associated with the 22q11.2 deletion syndrome,^{20–22,60,61} it is likely that defective PIKK biogenesis contributes to the pathophysiology of this disorder. In support of this possibility, mutations in *TELO2* and *TTI2* also cause intellectual disability disorders.^{82,83}

In addition to GNB1L, TELO2 also interacts with the PIH1D1 and RPAP3 proteins, which have also been implicated in PIKK biogenesis.¹⁴ PIH1D1 binds to the same region of TELO2 that associates with GNB1L, but mutations in the key phosphoacceptor residues (S487/S491) on TELO2 required for the PIH1D1 interaction did not affect GNB1L binding, indicating that GNB1L forms a complex with TELO2 independent of PIH1D1 (Figure S10G). Similarly, depletion of PIH1D1 and RPAP3 did not cause a marked decrease in PIKK protein levels in RKO *TP53*^{-/-} cells (Figure S10H), suggesting that the GNB1L-TTT-RUVBL1/2 pathway may be the dominant PIKK biogenesis route in human cells.

Limitations of the study

The study employed CRISPR screens using γ -H2AX formation as a readout to identify genes that suppress DNA damage accumulation in human cells. Although powerful, CRISPR screens have blind spots, and they need to be considered when interpreting results. In particular, false negatives are not uncommon and can be caused by the lack of efficient targeting, the presence of redundant genes such as paralogs, or simply the lack of guides targeting that particular gene. Furthermore, it is important to state that we used a marker of DNA damage, γ -H2AX, rather than monitoring DNA damage per se. Therefore, some of the genes scored in our screens may affect the formation or dephosphorylation of H2AX itself. Finally, γ -H2AX is not induced by every kind of DNA lesion similarly, and different readouts of DNA damage would certainly find overlapping as well as distinct gene sets.

STAR★METHODS

Detailed methods are provided in the online version of this paper and include the following:

- KEY RESOURCES TABLE
- RESOURCE AVAILABILITY
 - Lead contact
 - Materials availability

- Data and code availability
- **EXPERIMENTAL MODEL AND STUDY PARTICIPANT DETAILS**
- **METHOD DETAILS**
 - Cell culture
 - Plasmids and viral vectors
 - Immunofluorescence microscopy
 - Immunofluorescence and flow cytometry
 - Phenotypic CRISPR/Cas9 screens based on γ -H2AX
 - Immunoprecipitation
 - Parallel TurboID-based proximity labeling and affinity purification coupled to mass spectrometry
 - DNA fiber assay
 - Incucyte cell growth assay
 - dTAG-mediated protein degradation system
 - HaloTag label-switch experiments
 - POPcode mutagenesis screen
 - AlphaFold2 prediction of GNB1L-TELO2 interaction
 - GO-Figure!
 - FoldX and rolling window analysis
- **QUANTIFICATION AND STATISTICAL ANALYSIS**

SUPPLEMENTAL INFORMATION

Supplemental information can be found online at <https://doi.org/10.1016/j.molcel.2023.06.025>.

ACKNOWLEDGMENTS

We thank Rachel Szilard for critical reading of the manuscript and Junjie Chen for sharing results prior to their publication. We thank Laurence Pearl, Mohinder Pal, and Oscar Llorca for discussions on the TTT complex, Agnel Sfeir for RKO *TP53*^{-/-} cells, Benham Nabet for dTAG^V-1, Jordan Young for sending Cas9-expressing COL-hTERT cells, and Cassandra Wong for helping with MS data deposition. Y.Z. is supported by an Ontario Trillium Scholarship. This work was supported by grants from NIH (RM1HG010461 and UM1HG011989, to F.P.R.), from the Canadian Cancer Society (705644 to D.D.), and from the Canadian Institutes of Health Research (CIHR, grants PJT-180438 to D.D. and FDN159926 to F.P.R.).

AUTHOR CONTRIBUTIONS

Conceptualization, Y.Z., F.P.R., and D.D.; investigation, Y.Z., D.T., D.R.C., L.L., S.F., A.G.C., Z.-Y.L., and D.S.; writing – original draft, Y.Z. and D.D.; writing – review and editing, Y.Z. and D.D.; visualization, Y.Z., L.H., and D.S.; formal analysis, D.T., J.W., H.M., and L.H.; resources, A.N.K., J.J., A.-C.G., and F.P.R.; data curation, L.H.; supervision, J.J., A.-C.G., F.G.H., F.P.R., and D.D.; funding acquisition, F.P.R. and D.D.

DECLARATION OF INTERESTS

D.D. is a shareholder and advisor for Repare Therapeutics. A.-C.G. is a member of *Molecular Cell's* Advisory Board.

Received: September 25, 2022

Revised: April 18, 2023

Accepted: June 21, 2023

Published: July 20, 2023

REFERENCES

1. Liu, Q., Guntuku, S., Cui, X.S., Matsuoka, S., Cortez, D., Tamai, K., Luo, G., Carattini-Rivera, S., DeMayo, F., Bradley, A., et al. (2000). Chk1 is an essential kinase that is regulated by Atr and required for the G(2)/M DNA damage checkpoint. *Genes Dev.* *14*, 1448–1459.
2. Matsuoka, S., Ballif, B.A., Smogorzewska, A., McDonald, E.R., 3rd, Hurov, K.E., Luo, J., Bakalarski, C.E., Zhao, Z., Solimini, N., Lerenthal, Y., et al. (2007). ATM and ATR substrate analysis reveals extensive protein networks responsive to DNA damage. *Science* *316*, 1160–1166.
3. Couch, F.B., Bansbach, C.E., Driscoll, R., Luzwick, J.W., Glick, G.G., Bétous, R., Carroll, C.M., Jung, S.Y., Qin, J., Cimprich, K.A., and Cortez, D. (2013). ATR phosphorylates SMARCAL1 to prevent replication fork collapse. *Genes Dev.* *27*, 1610–1623. <https://doi.org/10.1101/gad.214080.113>.
4. Ward, I.M., and Chen, J. (2001). Histone H2AX is phosphorylated in an ATR-dependent manner in response to replicational stress. *J. Biol. Chem.* *276*, 47759–47762.
5. Kumagai, A., Lee, J., Yoo, H.Y., and Dunphy, W.G. (2006). TopBP1 activates the ATR-ATRIP complex. *Cell* *124*, 943–955. <https://doi.org/10.1016/j.cell.2005.12.041>.
6. Bass, T.E., Luzwick, J.W., Kavanaugh, G., Carroll, C., Dungrawala, H., Glick, G.G., Feldkamp, M.D., Putney, R., Chazin, W.J., and Cortez, D. (2016). ETAA1 acts at stalled replication forks to maintain genome integrity. *Nat. Cell Biol.* *18*, 1185–1195. <https://doi.org/10.1038/ncb3415>.
7. Haahr, P., Hoffmann, S., Tollenaere, M.A., Ho, T., Toledo, L.I., Mann, M., Bekker-Jensen, S., Räschele, M., and Mailand, N. (2016). Activation of the ATR kinase by the RPA-binding protein ETAA1. *Nat. Cell Biol.* *18*, 1196–1207. <https://doi.org/10.1038/ncb3422>.
8. Saldivar, J.C., Cortez, D., and Cimprich, K.A. (2017). The essential kinase ATR: ensuring faithful duplication of a challenging genome. *Nat. Rev. Mol. Cell Biol.* *18*, 622–636. <https://doi.org/10.1038/nrm.2017.67>.
9. Lempiäinen, H., and Halazonetis, T.D. (2009). Emerging common themes in regulation of PIKKs and PI3Ks. *EMBO J.* *28*, 3067–3073. <https://doi.org/10.1038/emboj.2009.281>.
10. Baretic, D., and Williams, R.L. (2014). PIKKs—the solenoid nest where partners and kinases meet. *Curr. Opin. Struct. Biol.* *29*, 134–142. <https://doi.org/10.1016/j.sbi.2014.11.003>.
11. Takai, H., Wang, R.C., Takai, K.K., Yang, H., and de Lange, T. (2007). Tel2 regulates the stability of PI3K-related protein kinases. *Cell* *131*, 1248–1259. <https://doi.org/10.1016/j.cell.2007.10.052>.
12. Takai, H., Xie, Y., de Lange, T., and Pavletich, N.P. (2010). Tel2 structure and function in the Hsp90-dependent maturation of mTOR and ATR complexes. *Genes Dev.* *24*, 1919–1930. <https://doi.org/10.1101/gad.1956410>.
13. Hurov, K.E., Cotta-Ramusino, C., and Elledge, S.J. (2010). A genetic screen identifies the Triple T complex required for DNA damage signaling and ATM and ATR stability. *Genes Dev.* *24*, 1939–1950. <https://doi.org/10.1101/gad.1934210>.
14. Horejsi, Z., Takai, H., Adelman, C.A., Collis, S.J., Flynn, H., Maslen, S., Skehel, J.M., de Lange, T., and Boulton, S.J. (2010). CK2 phospho-dependent binding of R2TP complex to TEL2 is essential for mTOR and SMG1 stability. *Mol. Cell* *39*, 839–850. <https://doi.org/10.1016/j.molcel.2010.08.037>.
15. Izumi, N., Yamashita, A., and Ohno, S. (2012). Integrated regulation of PIKK-mediated stress responses by AAA+ proteins RUVBL1 and RUVBL2. *Nucleus* *3*, 29–43. <https://doi.org/10.4161/nucl.18926>.
16. Olivieri, M., Cho, T., Álvarez-Quilón, A., Li, K., Schellenberg, M.J., Zimmermann, M., Hustedt, N., Rossi, S.E., Adam, S., Melo, H., et al. (2020). A genetic map of the response to DNA damage in human cells. *Cell* *182*, 481–496.e21. <https://doi.org/10.1016/j.cell.2020.05.040>.
17. Cheng, C.H., and Kuchta, R.D. (1993). DNA polymerase epsilon: aphidicolin inhibition and the relationship between polymerase and exonuclease activity. *Biochemistry* *32*, 8568–8574. <https://doi.org/10.1021/bi00084a025>.
18. Krakoff, I.H., Brown, N.C., and Reichard, P. (1968). Inhibition of ribonucleoside diphosphate reductase by hydroxyurea. *Cancer Res.* *28*, 1559–1565.

19. Harrington, C., and Perrino, F.W. (1995). The effects of cytosine arabinoside on RNA-primed DNA synthesis by DNA polymerase alpha-primase. *J. Biol. Chem.* *270*, 26664–26669. <https://doi.org/10.1074/jbc.270.44.26664>.
20. Williams, N.M., Glaser, B., Norton, N., Williams, H., Pierce, T., Moskvina, V., Monks, S., Del Favero, J., Goossens, D., Rujescu, D., et al. (2008). Strong evidence that GNB1L is associated with schizophrenia. *Hum. Mol. Genet.* *17*, 555–566. <https://doi.org/10.1093/hmg/ddm330>.
21. Paylor, R., Glaser, B., Mupo, A., Ataliotis, P., Spencer, C., Sobotka, A., Sparks, C., Choi, C.H., Oghalai, J., Curran, S., et al. (2006). Tbx1 haploinsufficiency is linked to behavioral disorders in mice and humans: implications for 22q11 deletion syndrome. *Proc. Natl. Acad. Sci. USA* *103*, 7729–7734. <https://doi.org/10.1073/pnas.0600206103>.
22. Chen, Y.Z., Matsushita, M., Girirajan, S., Lisowski, M., Sun, E., Sul, Y., Bernier, R., Estes, A., Dawson, G., Minshew, N., et al. (2012). Evidence for involvement of GNB1L in autism. *Am. J. Med. Genet. B Neuropsychiatr. Genet.* *159B*, 61–71. <https://doi.org/10.1002/ajmg.b.32002>.
23. Huang, X., and Darzynkiewicz, Z. (2006). Cytometric assessment of histone H2AX phosphorylation: a reporter of DNA damage. *Methods Mol. Biol.* *314*, 73–80. <https://doi.org/10.1385/1-59259-973-7-073>.
24. Rogakou, E.P., Pilch, D.R., Orr, A.H., Ivanova, V.S., and Bonner, W.M. (1998). DNA double-stranded breaks induce histone H2AX phosphorylation on serine 139. *J. Biol. Chem.* *273*, 5858–5868.
25. Hart, T., Tong, A.H.Y., Chan, K., Van Leeuwen, J., Seetharaman, A., Aregger, M., Chandrashekar, M., Hustedt, N., Seth, S., Noonan, A., et al. (2017). Evaluation and design of genome-wide CRISPR/SpCas9 knockout screens. *G3 (Bethesda)* *7*, 2719–2727. <https://doi.org/10.1534/g3.117.041277>.
26. Li, W., Xu, H., Xiao, T., Cong, L., Love, M.I., Zhang, F., Irizarry, R.A., Liu, J.S., Brown, M., and Liu, X.S. (2014). MAGeCK enables robust identification of essential genes from genome-scale CRISPR/Cas9 knockout screens. *Genome Biol.* *15*, 554. <https://doi.org/10.1186/s13059-014-0554-4>.
27. Szklarczyk, D., Gable, A.L., Nastou, K.C., Lyon, D., Kirsch, R., Pyysalo, S., Doncheva, N.T., Legeay, M., Fang, T., Bork, P., et al. (2021). The STRING database in 2021: customizable protein-protein networks, and functional characterization of user-uploaded gene/measurement sets. *Nucleic Acids Res.* *49*, D605–D612. <https://doi.org/10.1093/nar/gkaa1074>.
28. Hart, T., and Moffat, J. (2016). BAGEL: a computational framework for identifying essential genes from pooled library screens. *BMC Bioinformatics* *17*, 164. <https://doi.org/10.1186/s12859-016-1015-8>.
29. Wu, Q., Schapira, M., Arrowsmith, C.H., and Baryste-Lovejoy, D. (2021). Protein arginine methylation: from enigmatic functions to therapeutic targeting. *Nat. Rev. Drug Discov.* *20*, 509–530. <https://doi.org/10.1038/s41573-021-00159-8>.
30. Hart, T., Chandrashekar, M., Aregger, M., Steinhart, Z., Brown, K.R., MacLeod, G., Mis, M., Zimmermann, M., Fradet-Turcotte, A., Sun, S., et al. (2015). High-resolution CRISPR screens reveal fitness genes and genotype-specific cancer liabilities. *Cell* *163*, 1515–1526. <https://doi.org/10.1016/j.cell.2015.11.015>.
31. Srinivasan, V., Netz, D.J., Webert, H., Mascarenhas, J., Pierik, A.J., Michel, H., and Lill, R. (2007). Structure of the yeast WD40 domain protein Cia1, a component acting late in iron-sulfur protein biogenesis. *Structure* *15*, 1246–1257. <https://doi.org/10.1016/j.str.2007.08.009>.
32. Austin-Tse, C., Halbritter, J., Zariwala, M.A., Gilberti, R.M., Gee, H.Y., Hellman, N., Pathak, N., Liu, Y., Panizzi, J.R., Patel-King, R.S., et al. (2013). Zebrafish ciliopathy screen plus human mutational analysis identifies C21orf59 and CDC65 defects as causing primary ciliary dyskinesia. *Am. J. Hum. Genet.* *93*, 672–686. <https://doi.org/10.1016/j.ajhg.2013.08.015>.
33. Lin, R., Elf, S., Shan, C., Kang, H.B., Ji, Q., Zhou, L., Hitosugi, T., Zhang, L., Zhang, S., Seo, J.H., et al. (2015). 6-phosphogluconate dehydrogenase links oxidative PPP, lipogenesis and tumour growth by inhibiting LKB1-AMPK signalling. *Nat. Cell Biol.* *17*, 1484–1496. <https://doi.org/10.1038/ncb3255>.
34. Liu, Z.R. (2002). p68 RNA helicase is an essential human splicing factor that acts at the U1 snRNA-5' splice site duplex. *Mol. Cell. Biol.* *22*, 5443–5450. <https://doi.org/10.1128/MCB.22.15.5443-5450.2002>.
35. Wilson, B.J., Bates, G.J., Nicol, S.M., Gregory, D.J., Perkins, N.D., and Fuller-Pace, F.V. (2004). The p68 and p72 DEAD box RNA helicases interact with HDAC1 and repress transcription in a promoter-specific manner. *BMC Mol. Biol.* *5*, 11. <https://doi.org/10.1186/1471-2199-5-11>.
36. Liang, W.W., and Cheng, S.C. (2015). A novel mechanism for Prp5 function in prespliceosome formation and proofreading the branch site sequence. *Genes Dev.* *29*, 81–93. <https://doi.org/10.1101/gad.253708.114>.
37. Cuadrado, A., Corrado, N., Perdiguer, E., Lafarga, V., Muñoz-Canoves, P., and Nebreda, A.R. (2010). Essential role of p18Hamlet/SRCAP-mediated histone H2A.Z chromatin incorporation in muscle differentiation. *EMBO J.* *29*, 2014–2025. <https://doi.org/10.1038/emboj.2010.85>.
38. Zhao, B., Chen, Y., Jiang, N., Yang, L., Sun, S., Zhang, Y., Wen, Z., Ray, L., Liu, H., Hou, G., et al. (2019). Znhit1 controls intestinal stem cell maintenance by regulating H2A.Z incorporation. *Nat. Commun.* *10*, 1071. <https://doi.org/10.1038/s41467-019-09060-w>.
39. Lanctot, A.A., Peng, C.Y., Pawlisz, A.S., Joksimovic, M., and Feng, Y. (2013). Spatially dependent dynamic MAPK modulation by the Nde1-Lis1-Brap complex patterns mammalian CNS. *Dev. Cell* *25*, 241–255. <https://doi.org/10.1016/j.devcel.2013.04.006>.
40. Li, S., Ku, C.Y., Farmer, A.A., Cong, Y.S., Chen, C.F., and Lee, W.H. (1998). Identification of a novel cytoplasmic protein that specifically binds to nuclear localization signal motifs. *J. Biol. Chem.* *273*, 6183–6189. <https://doi.org/10.1074/jbc.273.11.6183>.
41. van der Meer, J.H., van der Poll, T., and van 't Veer, C. (2014). TAM receptors, Gas6, and protein S: roles in inflammation and hemostasis. *Blood* *123*, 2460–2469. <https://doi.org/10.1182/blood-2013-09-528752>.
42. Yu, Z., Mersaoui, S.Y., Guitton-Sert, L., Coulombe, Y., Song, J., Masson, J.Y., and Richard, S. (2020). DDX5 resolves R-loops at DNA double-strand breaks to promote DNA repair and avoid chromosomal deletions. *NAR Cancer* *2*, zcaa028. <https://doi.org/10.1093/narcan/zcaa028>.
43. Hernández-Pérez, S., Cabrera, E., Amoedo, H., Rodríguez-Acebes, S., Koundrioukoff, S., Debatisse, M., Méndez, J., and Freire, R. (2016). USP37 deubiquitinates Cdt1 and contributes to regulate DNA replication. *Mol. Oncol.* *10*, 1196–1206. <https://doi.org/10.1016/j.molonc.2016.05.008>.
44. Yeh, C., Coyaud, É., Bashkurov, M., van der Lelij, P., Cheung, S.W., Peters, J.M., Raught, B., and Pelletier, L. (2015). The deubiquitinase USP37 regulates chromosome cohesion and mitotic progression. *Curr. Biol.* *25*, 2290–2299. <https://doi.org/10.1016/j.cub.2015.07.025>.
45. Friesen, W.J., Wyce, A., Paushkin, S., Abel, L., Rappsilber, J., Mann, M., and Dreyfuss, G. (2002). A novel WD repeat protein component of the methylosome binds Sm proteins. *J. Biol. Chem.* *277*, 8243–8247. <https://doi.org/10.1074/jbc.M109984200>.
46. Lee, J.H., and Skalnik, D.G. (2008). Wdr82 is a C-terminal domain-binding protein that recruits the Setd1A histone H3-Lys4 methyltransferase complex to transcription start sites of transcribed human genes. *Mol. Cell. Biol.* *28*, 609–618. <https://doi.org/10.1128/MCB.01356-07>.
47. Cantor, S.B., Bell, D.W., Ganesan, S., Kass, E.M., Drapkin, R., Grossman, S., Wahrer, D.C., Sgroi, D.C., Lane, W.S., Haber, D.A., and Livingston, D.M. (2001). BACH1, a novel helicase-like protein, interacts directly with BRCA1 and contributes to its DNA repair function. *Cell* *105*, 149–160.
48. Quinet, A., Carvajal-Maldonado, D., Lemacon, D., and Vindigni, A. (2017). DNA fiber analysis: mind the gap! *Methods Enzymol.* *591*, 55–82. <https://doi.org/10.1016/bs.mie.2017.03.019>.
49. Peng, M., Cong, K., Panzarino, N.J., Nayak, S., Calvo, J., Deng, B., Zhu, L.J., Morocz, M., Hegedus, L., Haracska, L., et al. (2018). Opposing roles of FANCD1 and HLF1 protect forks and restrain replication during stress. *Cell Rep.* *24*, 3251–3261. <https://doi.org/10.1016/j.celrep.2018.08.065>.

50. Cong, K., Peng, M., Kousholt, A.N., Lee, W.T.C., Lee, S., Nayak, S., Kraiss, J., VanderVere-Carozza, P.S., Pawelczak, K.S., Calvo, J., et al. (2021). Replication gaps are a key determinant of PARP inhibitor synthetic lethality with BRCA deficiency. *Mol. Cell* *81*, 3128–3144.e7. <https://doi.org/10.1016/j.molcel.2021.06.011>.
51. Gallo, D., Kim, T., Szakal, B., Saayman, X., Narula, A., Park, Y., Branzei, D., Zhang, Z., and Brown, G.W. (2019). Rad5 recruits error-prone DNA polymerases for mutagenic repair of ssDNA gaps on undamaged templates. *Mol. Cell* *73*, 900–914.e9. <https://doi.org/10.1016/j.molcel.2019.01.001>.
52. Choe, K.N., and Moldovan, G.L. (2017). Forging ahead through darkness: PCNA, still the principal conductor at the replication fork. *Mol. Cell* *65*, 380–392. <https://doi.org/10.1016/j.molcel.2016.12.020>.
53. Peng, M., Litman, R., Xie, J., Sharma, S., Brosh, R.M., Jr., and Cantor, S.B. (2007). The FANCDJ/MutLalpha interaction is required for correction of the cross-link response in FA-J cells. *EMBO J.* *26*, 3238–3249. <https://doi.org/10.1038/sj.emboj.7601754>.
54. Yu, X., Chini, C.C.S., He, M., Mer, G., and Chen, J. (2003). The BRCT domain is a phospho-protein binding domain. *Science* *302*(5645), 639–642.
55. Gong, Z., Kim, J.E., Leung, C.C., Glover, J.N., and Chen, J. (2010). BACH1/FANCDJ acts with TopBP1 and participates early in DNA replication checkpoint control. *Mol. Cell* *37*, 438–446. <https://doi.org/10.1016/j.molcel.2010.01.002>.
56. Salleron, L., Magistrelli, G., Mary, C., Fischer, N., Bairoch, A., and Lane, L. (2014). DERA is the human deoxyribose phosphate aldolase and is involved in stress response. *Biochim. Biophys. Acta* *1843*, 2913–2925. <https://doi.org/10.1016/j.bbamcr.2014.09.007>.
57. Garcia, P.L., Liu, Y., Jiricny, J., West, S.C., and Janscak, P. (2004). Human RECQ5beta, a protein with DNA helicase and strand-annealing activities in a single polypeptide. *EMBO J.* *23*, 2882–2891. <https://doi.org/10.1038/sj.emboj.7600301>.
58. Schwendener, S., Raynard, S., Paliwal, S., Cheng, A., Kanagaraj, R., Shevelev, I., Stark, J.M., Sung, P., and Janscak, P. (2010). Physical interaction of RECQ5 helicase with RAD51 facilitates its anti-recombinase activity. *J. Biol. Chem.* *285*, 15739–15745. <https://doi.org/10.1074/jbc.M110.110478>.
59. Di Marco, S., Hasanova, Z., Kanagaraj, R., Chappidi, N., Altmannova, V., Menon, S., Sedlackova, H., Langhoff, J., Surendranath, K., Hühn, D., et al. (2017). RECQ5 helicase cooperates with MUS81 endonuclease in processing stalled replication forks at common fragile sites during mitosis. *Mol. Cell* *66*, 658–671.e8. <https://doi.org/10.1016/j.molcel.2017.05.006>.
60. Ishiguro, H., Koga, M., Horiuchi, Y., Noguchi, E., Morikawa, M., Suzuki, Y., Arai, M., Niizato, K., Iritani, S., Itokawa, M., et al. (2010). Supportive evidence for reduced expression of GNB1L in schizophrenia. *Schizophr. Bull.* *36*, 756–765. <https://doi.org/10.1093/schbul/sbn160>.
61. Gong, L., Liu, M., Jen, J., and Yeh, E.T. (2000). GNB1L, a gene deleted in the critical region for DiGeorge syndrome on 22q11, encodes a G-protein beta-subunit-like polypeptide. *Biochim. Biophys. Acta* *1494*, 185–188. [https://doi.org/10.1016/s0167-4781\(00\)00189-5](https://doi.org/10.1016/s0167-4781(00)00189-5).
62. Funke, B., Pandita, R.K., and Morrow, B.E. (2001). Isolation and characterization of a novel gene containing WD40 repeats from the region deleted in velo-cardio-facial/DiGeorge syndrome on chromosome 22q11. *Genomics* *73*, 264–271. <https://doi.org/10.1006/geno.2000.6506>.
63. Toledo, L.I., Altmeyer, M., Rask, M.B., Lukas, C., Larsen, D.H., Povlsen, L.K., Bekker-Jensen, S., Mailand, N., Bartek, J., and Lukas, J. (2013). ATR prohibits replication catastrophe by preventing global exhaustion of RPA. *Cell* *155*, 1088–1103. <https://doi.org/10.1016/j.cell.2013.10.043>.
64. Han, T., Goralski, M., Capota, E., Padrick, S.B., Kim, J., Xie, Y., and Nijhawani, D. (2016). The antitumor toxin CD437 is a direct inhibitor of DNA polymerase alpha. *Nat. Chem. Biol.* *12*, 511–515. <https://doi.org/10.1038/nchembio.2082>.
65. Ercilla, A., Benada, J., Amitash, S., Zonderland, G., Baldi, G., Somyajit, K., Ochs, F., Costanzo, V., Lukas, J., and Toledo, L. (2020). Physiological tolerance to ssDNA enables strand uncoupling during DNA replication. *Cell Rep.* *30*, 2416–2429.e7. <https://doi.org/10.1016/j.celrep.2020.01.067>.
66. Branon, T.C., Bosch, J.A., Sanchez, A.D., Udeshi, N.D., Svinkina, T., Carr, S.A., Feldman, J.L., Perrimon, N., and Ting, A.Y. (2018). Efficient proximity labeling in living cells and organisms with TurboID. *Nat. Biotechnol.* *36*, 880–887. <https://doi.org/10.1038/nbt.4201>.
67. Teo, G., Liu, G., Zhang, J., Nesvizhskii, A.I., Gingras, A.C., and Choi, H. (2014). SAINTexpress: improvements and additional features in Significance Analysis of interactome software. *J. Proteomics* *100*, 37–43. <https://doi.org/10.1016/j.jprot.2013.10.023>.
68. Machleidt, T., Woodrooffe, C.C., Schwinn, M.K., Méndez, J., Robers, M.B., Zimmerman, K., Otto, P., Daniels, D.L., Kirkland, T.A., and Wood, K.V. (2015). NanoBRET—a novel BRET platform for the analysis of protein-protein interactions. *ACS Chem. Biol.* *10*, 1797–1804. <https://doi.org/10.1021/acschembio.5b00143>.
69. Nabet, B., Roberts, J.M., Buckley, D.L., Paulk, J., Dastjerdi, S., Yang, A., Leggett, A.L., Erb, M.A., Lawlor, M.A., Souza, A., et al. (2018). The dTAG system for immediate and target-specific protein degradation. *Nat. Chem. Biol.* *14*, 431–441. <https://doi.org/10.1038/s41589-018-0021-8>.
70. Nabet, B., Ferguson, F.M., Seong, B.K.A., Kuljanin, M., Leggett, A.L., Mohardt, M.L., Robichaud, A., Conway, A.S., Buckley, D.L., Mancias, J.D., et al. (2020). Rapid and direct control of target protein levels with VHL-recruiting dTAG molecules. *Nat. Commun.* *11*, 4687. <https://doi.org/10.1038/s41467-020-18377-w>.
71. Fowler, D.M., and Fields, S. (2014). Deep mutational scanning: a new style of protein science. *Nat. Methods* *11*, 801–807. <https://doi.org/10.1038/nmeth.3027>.
72. Weile, J., Sun, S., Cote, A.G., Knapp, J., Verby, M., Mellor, J.C., Wu, Y., Pons, C., Wong, C., van Lieshout, N., et al. (2017). A framework for exhaustively mapping functional missense variants. *Mol. Syst. Biol.* *13*, 957. <https://doi.org/10.15252/msb.20177908>.
73. Sun, S., Weile, J., Verby, M., Wu, Y., Wang, Y., Cote, A.G., Fotiadou, I., Kitaygorodsky, J., Vidal, M., Rine, J., et al. (2020). A proactive genotype-to-patient-phenotype map for cystathionine beta-synthase. *Genome Med.* *12*, 13. <https://doi.org/10.1186/s13073-020-0711-1>.
74. Guerois, R., Nielsen, J.E., and Serrano, L. (2002). Predicting changes in the stability of proteins and protein complexes: a study of more than 1000 mutations. *J. Mol. Biol.* *320*, 369–387. [https://doi.org/10.1016/S0022-2836\(02\)00442-4](https://doi.org/10.1016/S0022-2836(02)00442-4).
75. Jumper, J., Evans, R., Pritzel, A., Green, T., Figurnov, M., Ronneberger, O., Tunyasuvunakool, K., Bates, R., Židek, A., Potapenko, A., et al. (2021). Highly accurate protein structure prediction with AlphaFold. *Nature* *596*, 583–589. <https://doi.org/10.1038/s41586-021-03819-2>.
76. Paul, V.D., and Lill, R. (2015). Biogenesis of cytosolic and nuclear iron-sulfur proteins and their role in genome stability. *Biochim. Biophys. Acta* *1853*, 1528–1539. <https://doi.org/10.1016/j.bbamcr.2014.12.018>.
77. Babbar, M., Basu, S., Yang, B., Croteau, D.L., and Bohr, V.A. (2020). Mitophagy and DNA damage signaling in human aging. *Mech. Ageing Dev.* *186*, 111207. <https://doi.org/10.1016/j.mad.2020.111207>.
78. Veatch, J.R., McMurray, M.A., Nelson, Z.W., and Gottschling, D.E. (2009). Mitochondrial dysfunction leads to nuclear genome instability via an iron-sulfur cluster defect. *Cell* *137*, 1247–1258. <https://doi.org/10.1016/j.cell.2009.04.014>.
79. Yaneva, D., Sparks, J.L., Donsbach, M., Zhao, S., Weickert, P., Bezalel-Buch, R., Stingle, J., and Walter, J.C. (2023). The FANCDJ helicase unfolds DNA-protein crosslinks to promote their repair. *Mol. Cell* *83*, 43–56.e10. <https://doi.org/10.1016/j.molcel.2022.12.005>.
80. Goto, G.H., Ogi, H., Biswas, H., Ghosh, A., Tanaka, S., and Sugimoto, K. (2017). Two separate pathways regulate protein stability of ATM/ATR-related protein kinases Mec1 and Tel1 in budding yeast. *PLoS Genet.* *13*, e1006873. <https://doi.org/10.1371/journal.pgen.1006873>.

81. Stirling, P.C., Bloom, M.S., Solanki-Patil, T., Smith, S., Sipahimalani, P., Li, Z., Kofoed, M., Ben-Aroya, S., Myung, K., and Hieter, P. (2011). The complete spectrum of yeast chromosome instability genes identifies candidate CIN cancer genes and functional roles for Astra complex components. *PLoS Genet.* *7*, e1002057. <https://doi.org/10.1371/journal.pgen.1002057>.
82. You, J., Sobreira, N.L., Gable, D.L., Jurgens, J., Grange, D.K., Belnap, N., Siniard, A., Szelinger, S., Schrauwen, I., Richholt, R.F., et al. (2016). A syndromic intellectual disability disorder caused by variants in *TELO2*, a gene encoding a component of the TTT complex. *Am. J. Hum. Genet.* *98*, 909–918. <https://doi.org/10.1016/j.ajhg.2016.03.014>.
83. Ziegler, A., Bader, P., McWalter, K., Douglas, G., Houdayer, C., Bris, C., Rouleau, S., Coutant, R., Colin, E., and Bonneau, D. (2019). Confirmation that variants in *TTI2* are responsible for autosomal recessive intellectual disability. *Clin. Genet.* *96*, 354–358. <https://doi.org/10.1111/cge.13603>.
84. Zimmermann, M., Murina, O., Reijns, M.A.M., Agathangelou, A., Challis, R., Tarnauskaitė, Ž., Muir, M., Fluteau, A., Aregger, M., McEwan, A., et al. (2018). CRISPR screens identify genomic ribonucleotides as a source of PARP-trapping lesions. *Nature* *559*, 285–289. <https://doi.org/10.1038/s41586-018-0291-z>.
85. Merrill, R.A., Song, J., Kephart, R.A., Klomp, A.J., Noack, C.E., and Strack, S. (2019). A robust and economical pulse-chase protocol to measure the turnover of HaloTag fusion proteins. *J. Biol. Chem.* *294*, 16164–16171. <https://doi.org/10.1074/jbc.RA119.010596>.
86. Weile, J., Kishore, N., Sun, S., Maaieh, R., Verby, M., Li, R., Fotiadou, I., Kitaygorodsky, J., Wu, Y., Hostenstein, A., et al. (2021). Shifting landscapes of human MTHFR missense-variant effects. *Am. J. Hum. Genet.* *108*, 1283–1300. <https://doi.org/10.1016/j.ajhg.2021.05.009>.
87. Mirdita, M., Schütze, K., Moriwaki, Y., Heo, L., Ovchinnikov, S., and Steinegger, M. (2022). ColabFold: making protein folding accessible to all. *Nat. Methods* *19*, 679–682. <https://doi.org/10.1038/s41592-022-01488-1>.
88. Evans, R., O'Neill, M., Pritzel, A., Antropova, N., Senior, A., Green, T., Židek, A., Bates, R., Blackwell, S., Yim, J., et al. (2022). Protein complex prediction with AlphaFold-Multimer. <https://doi.org/10.1101/2021.10.04.463034>.
89. Pettersen, E.F., Goddard, T.D., Huang, C.C., Meng, E.C., Couch, G.S., Croll, T.I., Morris, J.H., and Ferrin, T.E. (2021). UCSF ChimeraX: structure visualization for researchers, educators, and developers. *Protein Sci.* *30*, 70–82. <https://doi.org/10.1002/pro.3943>.

STAR★METHODS

KEY RESOURCES TABLE

REAGENT or RESOURCE	SOURCE	IDENTIFIER
Antibodies		
Polyclonal rabbit anti-H2AX	Cell Signaling	Cat#2595; RRID:AB_10694556
Monoclonal mouse anti- γ -H2AX	Millipore	Cat#05-636; RRID:AB_309864
Monoclonal mouse anti- γ -H2AX-Alexa Fluor 647	Millipore	Cat#05-636-AF647
Polyclonal rabbit anti- γ -H2AX	Cell Signaling	Cat#2577; RRID:AB_2118010
Polyclonal rabbit anti-53BP1	Santa Cruz	Cat#sc22760; RRID:AB_2256326
Monoclonal mouse anti-RPA2	Abcam	Cat#ab2175; RRID:AB_302873
Polyclonal rabbit anti-pRPA2 (S33)	Bethyl Laboratories	Cat#A300-246A-3; RRID:AB_2180847
Monoclonal mouse anti-CHK1	Santa Cruz	Cat#sc8408; RRID:AB_627257
Monoclonal rabbit anti-pCHK1 (S345)	Cell Signaling	Cat#2348; RRID:AB_331212
Monoclonal mouse anti-PCNA	Santa Cruz	Cat#sc56; RRID:AB_628110
Polyclonal rabbit anti-ubiquityl PCNA (Lys164)	Cell Signaling	Cat#2577; RRID:AB_2118010
Polyclonal rabbit anti-GNB1L	Sigma-Aldrich	Cat#HPA034627; RRID:AB_10600662
Polyclonal rabbit anti-TELO2	Proteintech	Cat#15975-1-AP; RRID:AB_2203337
Polyclonal rabbit anti-TTI1	Bethyl Laboratories	Cat#A303-451A; RRID:AB_10953982
Polyclonal rabbit anti-TTI2	Bethyl Laboratories	Cat#A303-476A; RRID:AB_10948973
Polyclonal rabbit anti-RUVBL1	Proteintech	Cat#10210-2-AP; RRID:AB_2184405
Polyclonal anti-RUVBL2	Abcam	Cat#ab36569; RRID:AB_2301439
Polyclonal rabbit anti-PIH1D1	Proteintech	Cat#19427-1-AP; RRID:AB_10640423
Polyclonal rabbit anti-RPAP3	Bethyl Laboratories	Cat#A304-854A-T; RRID:AB_2621049
Polyclonal goat anti-ATR	Santa Cruz	Cat#sc1887; RRID:AB_630893
Polyclonal goat anti-DNA-PKcs	Santa Cruz	Cat#sc1552; RRID:AB_2172847
Monoclonal rabbit anti-ATM	Cell Signaling	Cat#2873; RRID:AB_2062659
Monoclonal rabbit anti-mTOR	Cell Signaling	Cat#2983; RRID:AB_2105622
Polyclonal rabbit anti-TRRAP	Bethyl Laboratories	Cat#A301-132A; RRID:AB_2209668
Polyclonal rabbit anti-SMG1	Bethyl Laboratories	Cat#A300-394A; RRID:AB_386105
Monoclonal mouse anti- α -Actinin	Millipore	Cat#05-384; RRID:AB_309709
Monoclonal mouse anti- α -Tubulin	Calbiochem	Cat#CP06; RRID:AB_2617116
Monoclonal mouse anti-GAPDH	Sigma-Aldrich	Cat#G9545; RRID:AB_796208
Polyclonal rabbit anti-GFP	Gift from Laurence Pelletier	N/A
Monoclonal rat anti-HA	Roche	Cat#ROAHAHA; RRID:AB_2687407
Monoclonal mouse anti-Flag M2-Peroxidase (HRP)	Sigma-Aldrich	Cat#A8592; RRID:AB_439702
Monoclonal rat anti-BrdU [BU1/75 (ICR1)]	Abcam	Cat#ab6326; RRID:AB_305426
Monoclonal mouse anti-BrdU (B44)	BD Biosciences	Cat#347580; RRID:AB_10015219
Polyclonal rabbit anti-RECQL5	Abcam	Cat#ab91422; RRID:AB_2050245
Monoclonal rabbit anti-FANCF	R&D Systems	Cat#MAB6496; RRID:AB_10719145
Polyclonal rabbit anti-DEA	Sigma-Aldrich	Cat#HPA055897; RRID:AB_2682963
Monoclonal HRP-sheep anti-mouse IgG	Cytiva	Cat#NA9310-1ml; RRID:AB_772193
Polyclonal HRP-goat anti-rabbit IgG	Jackson ImmunoResearch Labs	Cat#111-035-144; RRID:AB_2307391
Polyclonal HRP-bovine anti-goat IgG	Jackson ImmunoResearch Labs	Cat#805-035-180; RRID:AB_2340874
Polyclonal Alexa Fluor 488-donkey anti rat IgG	Thermo Fisher	Cat#A21208; RRID:AB_2535794
Polyclonal Alexa Fluor 555-donkey anti mouse IgG	Thermo Fisher	Cat#A31570; RRID:AB_2536180
Polyclonal Alexa Fluor 488-goat anti mouse IgG	Thermo Fisher	Cat#A11029; RRID:AB_2534088
Polyclonal Alexa Fluor 647-goat anti mouse IgG	Thermo Fisher	Cat#A21236; RRID:AB_2535805

(Continued on next page)

Continued		
REAGENT or RESOURCE	SOURCE	IDENTIFIER
Polyclonal Alexa Fluor 488-goat anti rabbit IgG	Thermo Fisher	Cat#A11034; RRID:AB_2576217
Polyclonal Alexa Fluor 647-goat anti rabbit IgG	Thermo Fisher	Cat#A21244; RRID:AB_2535812
Bacterial and virus strains		
XL1-Blue competent cells	Agilent	Cat#200249
Chemicals, peptides, and recombinant proteins		
Lipofectamine 2000	Thermo Fisher	Cat#11668030
Lipofectamine RNAiMAX	Thermo Fisher	Cat#13778100
Puromycin	InvivoGen	Cat#ant-pr
Blasticidin	InvivoGen	Cat#ant-bl
Nourseothricin (clonNAT)	Gold Biotechnology	Cat#N-500-5
Polybrene	Sigma-Aldrich	Cat#TR-1003
Penicillin and streptomycin (Pen Strep)	GIBCO	Cat#15140122
Fetal Bovine Serum (FBS)	Wisent Bioproduct	Cat#080-150
Phosphate Buffer Saline (PBS)	GIBCO	Cat#10010023
Dulbecco's Modified Eagle's Medium (DMEM)	GIBCO	Cat#C11965500BT
Trypsin	Sigma-Aldrich	Cat#T1426
FLAG M2 Magnetic Beads	Millipore	Cat#M8823-5ML
ChromoTek GFP-Trap® Magnetic Agarose	Proteintech	Cat#gtma
Streptavidin Sepharose High Performance	Cytiva	Cat#17-5113-01
Aphidicolin	Focus Biochemicals	Cat#10-2058
Hydroxyurea	Sigma-Aldrich	Cat#H8627
Ara-C	Sigma-Aldrich	Cat#C1768
CD437	Sigma-Aldrich	Cat#C5865
Gemcitabine	Cayman chemical	Cat#9003096
dTAG ^V -1	Gift from Benham Nabet (PMID: 32948771)	N/A
TBB (4,5,6,7-tetrabromobenzotriazole)	Selleckchem	Cat#S5265
PF-06873600	MedChemExpress	Cat#HY-114177
TAK-931	Chemietek	Cat#CT-TAK931
5-Chloro-2'-deoxyuridine (CldU)	Sigma-Aldrich	Cat#C6891
5-Iodo-2'-deoxyuridine (IdU)	Sigma-Aldrich	Cat#I7125
ProLong Gold Antifade Mountant	Invitrogen	Cat#P36930
Critical commercial assays		
QIAamp Blood Maxi Kit	QIAGEN	Cat#51194
Q5 High-Fidelity 2X Master Mix	New England Biolabs	Cat#M5044L
NextSeq 500/550 High Output Kit v2.5	Illumina	Cat#20024906
NanoBRET™ PPI Starter Systems	Promega	N1811
TaqMan Gene Expression Assay of <i>ATM</i>	Thermo Fisher	Cat#Hs00175892_m1
TaqMan Gene Expression Assay of <i>ATR</i>	Thermo Fisher	Cat#Hs00992123_m1
TaqMan Gene Expression Assay of <i>PRKDC</i>	Thermo Fisher	Cat#Hs00179161_m1
Deposited data		
Raw sequencing reads of the CRISPR screens	This paper	BioProject: PRJNA948427
Raw image data	This paper	Mendeley data: https://doi.org/10.17632/z4ht3txn2k.1
Original code	This paper	Zenodo: https://doi.org/10.5281/zenodo.7833858
Proteomics data	This paper	ProteomeXchange: PXD043028/ PXD043029
Experimental models: Cell lines		
Human: RPE1-hTERT Cas9 <i>TP53</i> ^{-/-}	PMID: 29973717	N/A

(Continued on next page)

Continued

REAGENT or RESOURCE	SOURCE	IDENTIFIER
Human: RPE1-hTERT Cas9 <i>TP53</i> ^{-/-} <i>FANCI-K1</i> clones	Gift from Arne Nedergaard Kousholt	Table S4
Human: 293T	ATCC	Cat#CRL-3216
Human: COL-hTERT	abmGood	Cat#T0570
Human: COL-hTERT Cas9 <i>TP53</i> ^{-/-}	Gift from Repare Therapeutics	N/A
Human: RKO <i>TP53</i> ^{-/-}	Gift from Agnel Sfeir	N/A
Human: RKO <i>TP53</i> ^{-/-} <i>FANCI-KO#1</i>	This paper	N/A
Human: RKO <i>TP53</i> ^{-/-} <i>FANCI-KO#2</i>	This paper	N/A
Human: RKO <i>TP53</i> ^{-/-} <i>RECQL5-KO#1</i>	This paper	N/A
Human: RKO <i>TP53</i> ^{-/-} <i>RECQL5-KO#2</i>	This paper	N/A
Oligonucleotides		
TKOv3 CRISPR libraries	PMID: 28655737	N/A
PCR#1 library primer forward V3_2_F: CTGCGTGCGCCAATTCTG	PMID: 32516598	N/A
PCR#2 library primer reverse V3_1_R2: AGAACCGGTCCTGTGTTCTG	PMID: 32516598	N/A
sgRNA sequences and TIDE PCR primers	This paper	Table S4
Recombinant DNA		
LentiCRISPRv2	PMID: 25075903	Addgene Cat#52961
pVSVg	PMID: 12717450	Addgene Cat#14888
pRSV-Rev	PMID: 9765382	Addgene Cat#12253
pMDLg/pRRE	PMID: 9765382	Addgene Cat#12251
pHIV-NAT-T2A-hCD52	Gift from R. Scully.	N/A
pHIV-NAT-T2A-hCD52-FANCI	This paper	N/A
pHIV-NAT-T2A-hCD52-FANCI-K52R	This paper	N/A
pHIV-NAT-T2A-hCD52-FANCI-K141A/K142A	This paper	N/A
pHIV-NAT-T2A-hCD52-FANCI-M299I	This paper	N/A
pHIV-NAT-T2A-hCD52-FANCI-R707C	This paper	N/A
pHIV-NAT-T2A-hCD52-FANCI-S990A	This paper	N/A
pHIV-NAT-T2A-hCD52-FANCI-T1133A	This paper	N/A
pHIV-NAT-T2A-hCD52-DEFA	This paper	N/A
pHIV-NAT-T2A-hCD52-DEFA-K254A	This paper	N/A
pHIV-NAT-T2A-hCD52-RECQL5-K58R	This paper	N/A
pHIV-NAT-T2A-hCD52-RECQL5-E584D	This paper	N/A
pHIV-NAT-T2A-hCD52-RECQL5-F666A	This paper	N/A
pHIV-NAT-T2A-hCD52-RECQL5-S727A	This paper	N/A
pHIV-NAT-T2A-hCD52-RECQL5	This paper	N/A
pHIV-NAT-T2A-hCD52-RECQL5(1-490)	This paper	N/A
pHIV-NAT-T2A-hCD52-RECQL5(1-620)	This paper	N/A
pHIV-NAT-T2A-hCD52-RECQL5(1-900)	This paper	N/A
pHIV-NAT-T2A-hCD52-RECQL5(491-991)	This paper	N/A
pHIV-NAT-T2A-hCD52-RECQL5(491-900)	This paper	N/A
pHIV-NAT-T2A-hCD52-RECQL5(621-900)	This paper	N/A
pHIV-NAT-T2A-hCD52-TELO2-N1(1-460)	This paper	N/A
pHIV-NAT-T2A-hCD52-TELO2-N2(1-640)	This paper	N/A
pHIV-NAT-T2A-hCD52-TELO2-C1(640-837)	This paper	N/A
pHIV-NAT-T2A-hCD52-TELO2-C2(460-837)	This paper	N/A
pHIV-NAT-T2A-hCD52-TELO2-C3(460-640)	This paper	N/A

(Continued on next page)

Continued

REAGENT or RESOURCE	SOURCE	IDENTIFIER
pHIV-NAT-T2A-hCD52-TELO2-C4(460-545)	This paper	N/A
pHIV-NAT-T2A-hCD52-TELO2-del1(Δ 460-545)	This paper	N/A
pHIV-NAT-T2A-hCD52-TELO2-del2(Δ 482-545)	This paper	N/A
pHIV-NAT-T2A-hCD52-TELO2-M1(⁴⁹⁰ DSDD ⁴⁹³ -AAAA)	This paper	N/A
pHIV-NAT-T2A-hCD52-TELO2-M2(⁴⁹⁸ YDMS ⁵⁰¹ -AAAA)	This paper	N/A
pHIV-NAT-T2A-hCD52-TELO2-M3(⁶⁰³ DRE ⁵⁰⁵ -AAA)	This paper	N/A
pHIV-NAT-T2A-hCD52-TELO2-M4(⁵¹⁶ RDC ⁵¹⁸ -AAA)	This paper	N/A
pcDNA5-FRT/TO-3xFLAG	LTRI OpenFreezer	Cat#V4978
pcDNA5-FRT/TO-3xFLAG-GNB1L	This paper	N/A
pcDNA5-miniTurbo-3xFLAG	Gift from Anne-Claude Gingras	N/A
pcDNA5-miniTurbo-3xFLAG-EGFP	Gift from Anne-Claude Gingras	N/A
pcDNA5-miniTurbo-3xFLAG-GNB1L	This paper	N/A
pLVU/GFP	PMID: 20132838	Addgene Cat#24177
pLVU/GFP-GNB1L	This paper	N/A
pLVU/GFP-GNB1L-S42L	This paper	N/A
pLVU/GFP-GNB1L-G43M	This paper	N/A
pLVU/GFP-GNB1L-A271E	This paper	N/A
pLVU/GFP-GNB1L-G272R	This paper	N/A
pLVU/GFP-GNB1L-D274G	This paper	N/A
pLVU/GFP-GNB1L-D315R	This paper	N/A
pLEX_305-N-dTAG	PMID: 29581585	Addgene Cat#91797
pLEX_305-N-dTAG-GNB1L	This paper	N/A
pNLF1-N-Nanoluc-CMV	Promega	N1811
NLF1-N-Nanoluc-CMV-GNB1L	This paper	N/A
pHTN HaloTag CMV-neo	Promega	Cat#G7721
pHTN HaloTag CMV-neo-ATR	This paper	N/A
pHTN HaloTag CMV-neo-TELO2	This paper	N/A
pHTC HaloTag CMV-neo	Promega	Cat#G7711
pHTC HaloTag CMV-neo-TELO2	This paper	N/A
pHTC HaloTag CMV-neo-TELO2-del1(Δ 460-545)	This paper	N/A
pHTC HaloTag CMV-neo-TELO2-del2(Δ 482-545)	This paper	N/A
pHTC HaloTag CMV-neo-TELO2-M1(⁴⁹⁰ DSDD ⁴⁹³ -AAAA)	This paper	N/A
pHTC HaloTag CMV-neo-TELO2-M2(⁴⁹⁸ YDMS ⁵⁰¹ -AAAA)	This paper	N/A
pHTC HaloTag CMV-neo-TELO2-M3(⁶⁰³ DRE ⁵⁰⁵ -AAA)	This paper	N/A
pHTC HaloTag CMV-neo-TELO2-M4(⁵¹⁶ RDC ⁵¹⁸ -AAA)	This paper	N/A

Software and algorithms

Cytoscape version 3.8.2	Cytoscape	https://cytoscape.org
R version 4.1.2	R software	https://www.r-project.org
MAGECK	PMID: 25476604	https://sourceforge.net/p/mageck/wiki/Home
BAGEL	PMID: 28655737	https://github.com/hart-lab/bagel/blob/master/BAGEL.py

(Continued on next page)

Continued

REAGENT or RESOURCE	SOURCE	IDENTIFIER
Adobe Illustrator CS6 (version 26.2.1)	Adobe Inc.	https://www.adobe.com/products/illustrator.html
Prism version 9.2.0	GraphPad	http://www.graphpad.com/scientific-software/prism/
ggplot2 (version 3.2.1)	N/A	https://ggplot2.tidyverse.org
FlowJo 10.5.3	FlowJo LLC	https://www.flowjo.com/
ImageJ Fiji	PMID: 22930834	https://imagej.net/Fiji
ChimeraX 1.3	PMID: 15264254	https://www.cgl.ucsf.edu/chimera/
LI-COR Image Studio 5.2	LI-COR Biosciences	https://www.licor.com/bio/image-studio/
Columbus Image Data Storage and Analysis	PerkinElmer	https://www.perkinelmer.com/product/image-data-storage-and-analysis-system-columbus

RESOURCE AVAILABILITY

Lead contact

Further information and requests for resources and reagents should be directed to and will be fulfilled by Daniel Durocher (durocher@lunenfeld.ca).

Materials availability

Materials included in this manuscript will be shared upon request.

Data and code availability

- The datasets generated and analyzed during this study are available at Mendeley data <https://doi.org/10.17632/z4ht3txn2k.1>, NCBI BioProject: PRJNA948427, and ProteomeXchange: PXD043028, PXD043029. These data are publicly available as of the date of publication.
- All original code generated in this study is available at Zenodo (<https://doi.org/10.5281/zenodo.7833858>) and are publicly available as of the date of publication.
- Any additional information required to reanalyze the data reported in this paper is available from the [lead contact](#) upon request.

EXPERIMENTAL MODEL AND STUDY PARTICIPANT DETAILS

Human cell lines used in this manuscript are summarized in the [key resources table](#).

METHOD DETAILS

Cell culture

RKO *TP53*^{-/-}, RPE1-hTERT *TP53*^{-/-}, COL-hTERT *TP53*^{-/-} and 293T cells were grown in Dulbecco's Modified Eagle Medium (DMEM; Gibco/Thermo Fisher) supplemented with 10% fetal bovine serum (FBS; Wisent), 1x non-essential amino acids, 200 mM GlutaMAX (both Gibco/Thermo Fisher), 100 U/ml penicillin and 100 µg/ml streptomycin (Pen/Strep; Wisent). All cell lines were routinely authenticated by STR and tested negative for mycoplasma.

RKO *TP53*^{-/-} *FANCL*-KO and *RECQL5*-KO gene knockouts were generated by electroporation of Cas9 and sgRNA using a Lonza Amaxa II nucleofector. sgRNA target sequences were: *FANCL*, AGATTACTAGAGAGCTCCGG; *RECQL5*, AGTCAGCTTCCTGATCAGGA. Cells were cultured for an additional five days after electroporation to provide time for gene editing and then seeded at low densities (500 cells/15-cm dish) for single-clone isolation. *FANCL*-KO and *RECQL5*-KO cell clones were identified by PCR amplification and ICE analysis (<https://ice.synthego.com>) and confirmed by immunoblot analysis (Table S4).

For the RPE1-hTERT *TP53*^{-/-} *FANCL* knock-in cell lines, the desired *FANCL* gene variants (K52R, K141/142A, S990A, T1133A) were introduced in the RPE1-hTERT *TP53*^{-/-} Cas9-expressing clone, using the RNP CRISPR approach of IDT. Sequences of PCR primers, sgRNA, and ssODN repair templates can be found in Table S4. The expression of *FANCL* variants were confirmed by immunoblot analysis.

Plasmids and viral vectors

DNA corresponding to sgRNAs was cloned into LentiCRISPRv2 using BamHI (Addgene, #52961). sgRNA target sequences and their validations can be found in Table S4. Lentiviral particles were produced in 293T cells by co-transfection of the targeting vector with vectors expressing VSV-G, RRE and REV using calcium phosphate. Medium was refreshed 12-16 h later. Virus-containing

supernatant was collected 36–40 h post transfection, cleared through a 0.4- μ m filter, supplemented with 8 μ g/ml polybrene (Sigma) and used for infection of target cells. The coding sequences for FANCI, RECQL5, GNB1L, TELO2, ATR were obtained from the OR-Feome collection (<http://horfdb.dfci.harvard.edu/>), archived in OpenFreezer. The coding sequences for FANCI, RECQL5, TELO2 were cloned into pHIV-NAT-T2A-hCD52 using NotI/XmaI restriction enzyme sites. The GNB1L coding sequence was cloned into pcDNA5-FRT/TO-3xFLAG, pcDNA5-miniTurbo-3xFLAG, pLVU/GFP, and pLEX_305-N-dTAG vectors using the Gateway system (Life Technologies/Thermo Fisher) according to the manufacturer's protocol. The TELO2 and ATR coding sequences were cloned into pHTN HaloTag CMV-neo using SbfI/NotI restriction enzyme sites. The TELO2 coding sequence was cloned into pHTC HaloTag CMV-neo using SbfI/PvuII restriction enzyme sites.

Immunofluorescence microscopy

To analyze γ -H2AX and 53BP1 focus formation in RKO *TP53*^{-/-} cell lines, cells were seeded on coverslips to grow for 24 h, and then subjected to the indicated treatments or left untreated. Cells were rinsed with PBS once, subsequently fixed with 4% paraformaldehyde (PFA, Thermo Fisher) for 15 min at room temperature, and permeabilized with 0.3% Triton X-100 (Sigma, T8787) for 30 min. After fixation, cells were rinsed with PBS for three times, blocked in blocking buffer (10% goat serum (Sigma, G6767), 0.5% NP-40 (Sigma-Aldrich, I3021), 5% w/v saponin (Sigma-Aldrich, 84510), diluted in PBS) for 30 min, incubated with primary antibodies (mouse anti- γ -H2AX JBW301 1:2500 and rabbit anti-53BP1 1:2500) diluted in blocking buffer for 2 h at room temperature. Cells were then washed three times in PBS for 5 min and stained with secondary antibodies (Alexa Fluor 488-conjugated goat anti-mouse IgG and Alexa Fluor 647-conjugated goat anti-rabbit IgG, 1:1000 in blocking buffer) and 0.5–0.8 μ g/mL DAPI (4,6-diamidino-2-phenylindole, Sigma-Aldrich, D9542) for 1 h at room temperature. Cells were washed as above, mounted in Pro-Long Gold mounting medium (Life Technologies), and imaged using a Zeiss LSM780 laser scanning microscope with a 60X objective. Image analysis was performed using Columbus (PerkinElmer) to quantify the nuclear foci of γ -H2AX and 53BP1 as described previously.¹⁶

For immunofluorescence analysis of γ -H2AX and RPA2 in RKO *TP53*^{-/-} cell lines, cells were grown on coverslips for 24 h, subjected to the indicated treatment, then pre-extracted for 10 min on ice with ice-cold buffer (25 mM HEPES, pH 7.4, 50 mM NaCl, 1 mM EDTA, 3 mM MgCl₂, 300 mM sucrose and 0.5% Triton X-100) and fixed with 4% PFA for 15 min at room temperature. Staining was as described before except the primary antibodies used were rabbit anti- γ -H2AX 1:200 and mouse anti-RPA2 1:500. Images were acquired on a Zeiss LSM780 laser scanning microscope with a 20X objective and analyzed by Columbus (PerkinElmer) to quantify the nuclear intensity of γ -H2AX and RPA2 signals.

Immunofluorescence and flow cytometry

Flow cytometry experiments were performed as described previously.⁸⁴ Briefly, cells were plated on 6-cm dishes to grow for 24 h before adding drugs. After drug treatment, cells were collected by trypsinization and centrifuged in a conical tube. Pellets were washed in PBS once and fixed in 4% PFA for 10 min at room temperature. Cells were spun, resuspended in 100 μ l PBS and chilled on ice for 1 min. 900 μ l of -20°C methanol was then added dropwise while gently vortexing. Fixed cells were stored at -20°C overnight or longer. Before staining, cells were spun down, washed with PBS, and blocked in blocking buffer (see “immunofluorescence microscopy” section) at room temperature for 30 min. Cells were then centrifuged and resuspended in diluted Alexa Fluor 647-conjugated mouse anti- γ -H2AX antibody (Millipore, 05-636-AF647, 1:1000 in blocking buffer). After 2 h incubation the antibody was diluted with 10X volume PBS, cells were spun down and resuspended in PBS with DAPI. Cells were analyzed on BD LSRFortessa X-20 (BD Biosciences), or MoFlo Astrios EQ Cell Sorter (Beckman Coulter), or Attune NxT/CytKick Max autosampler (Thermo Fisher).

Phenotypic CRISPR/Cas9 screens based on γ -H2AX

RKO *TP53*^{-/-} cells or COL-hTERT *TP53*^{-/-} cells were transduced with the lentiviral TKOv3 library²⁵ at a low MOI (\sim 0.3) and puromycin-containing medium was added the next day. Three days after transduction, which was considered the initial time point (T0), cells were pooled together and divided in two technical replicates (the only exception is the untreated RKO screen in which we did four replicates). Each replicate was cultured for five more days to provide time for sgRNA-mediated gene editing, then divided into different treatments at T5. Cells were either treated with 0.3 μ M Aph, or with 0.2 μ M Ara-C, or with 200 μ M HU, or left untreated (UT) for 24 h. At T6, 40 million cells per sample were collected in pellets and frozen at -80°C as the unsorted population, with the remaining cells (\sim 400 million) subjected to fixation, staining and FACS. These cells were spun down in 50 ml conical tubes, washed with PBS once, and fixed in 4% PFA for 10 min at room temperature while rotating. Cells were then pelleted and resuspended in 1 ml PBS and chilled on ice. 19 ml of -20°C methanol was then added dropwise while gently vortexing. Fixed cells were stored at -20°C overnight or longer. Before staining, cells were spun down, washed with FACS buffer (PBS with 5% FBS), and blocked in blocking buffer at room temperature for 30 min while rotating. Cells were then centrifuged and resuspended in diluted Alexa Fluor 647-conjugated mouse anti- γ -H2AX antibody (Millipore, 05-636-AF647, 1:1000 in blocking buffer). After 2 h incubation, 40 ml of FACS buffer was added, cells were spun down and resuspended in 10 ml PBS with DAPI, then subjected to sorting on a MoFlo Astrios EQ Cell Sorter. Cells with the top 5% of γ -H2AX signal intensity were collected and their genomic DNA (gDNA) was extracted using the FFPE DNA Purification Kit (Norgen Biotek Cat. 47400). gDNA from unsorted cell population was isolated using the QIAamp Blood Maxi Kit (Qiagen). For both sorted and the unsorted cell populations, genome-integrated sgRNA sequences were amplified by PCR using KAPA HiFi HotStart ReadyMix (Kapa Biosystems). i5 and i7 multiplexing barcodes were added in a second round of PCR and final gel-purified products were sequenced on Illumina NextSeq500 systems to determine sgRNA representation in each sample.

Immunoprecipitation

Cells were transfected with pcDNA5-3xFLAG-TELO2. 48 hours later, cells were collected by trypsinization, washed with PBS once, and lysed in 1 ml high salt lysis buffer (50 mM HEPES pH8, 300 mM NaCl, 2 mM EDTA, 0.1% NP-40, 10% glycerol, plus protease inhibitors (cOmplete EDTA-free protease inhibitor cocktail, Roche, 11836170001)). Lysates were incubated with gentle rotation at 4°C for 30 min with occasional vortexing and then centrifuged at 15,000xg for 10 min. 150 μ l of total cell lysates were used as input and 850 μ l were incubated with 40 μ l anti-FLAG M2 magnetic bead (Sigma M8233) at 4°C overnight while rotating. Beads were washed three times with TBS (50 mM Tris-HCl pH 7.4, 150 mM NaCl) and eluted with 100 μ l of 3x FLAG peptide (100 μ g/ml, GLPbio, GP10149) at 4°C for 30 min. Elution was repeated once more and 40 μ l 6x SDS-PAGE sample buffer was added to each sample. Samples were boiled at 95°C for 5 min and subjected to SDS-PAGE and immunoblot analysis.

Parallel TurboID-based proximity labeling and affinity purification coupled to mass spectrometry

Parental 293 Flp-In cells, and cells stably expressing miniTurbo-3xFlag-GNB1L, miniTurbo-3xFlag-eGFP or miniTurbo-3xFlag were used for parallel miniTurbo and AP-MS studies. For both TurboID and AP-MS, two 150-mm plates of cells were treated with 5 μ g/ml doxycycline for 24 h to induce expression of bait proteins. For miniTurbo, 50 μ M biotin was added to cells 40 min before harvest. Cells were pelleted at low speed, washed with ice-cold PBS and frozen at -80°C until purification. Cell lysis, purification, and mass spectrometry were performed as previously described in (PMID: 29991506). For TurboID, cells were lysed in 1.5 ml of modified RIPA buffer [50 mM Tris-HCl, pH 7.4, 150 mM NaCl, 1 mM EGTA, 0.5 mM EDTA, 1 mM MgCl₂, 1% NP40, 0.1% SDS, 0.4% sodium deoxycholate, 1 mM PMSF and 1x Protease Inhibitor mixture (Sigma-Aldrich, Cat# P8340)]. Cells were sonicated and added with 250 U of TurboNuclease (BioVision Inc., Milpitas, CA, Cat# 9207) and 10 μ g of RNase A (Bio Basic, Markham, ON, Canada, Cat# RB0473). The SDS concentration was increased to 0.4% and the samples were rotated at 4 °C for 5 min. Samples were centrifuged at 15,000 g for 15 min and the supernatant was used for biotinylated protein capture using 30 μ l of pre-washed Streptavidin agarose beads (GE Healthcare Life Science, Cat# 17511301). After 4 h, the beads were washed once with SDS-Wash buffer, twice with RIPA wash buffer, once with TNNE buffer, and three times with 50 mM ammonium bicarbonate (ABC buffer), pH 8.0. On-bead digestion was performed with 1 μ g of trypsin (Sigma Aldrich, Cat# 6567) in 70 μ l of ABC buffer, overnight at 37 °C, followed by further digestion with an additional 0.5 μ g of trypsin for 3 h. Supernatants were collected into a new tube. Beads were washed twice with water and this supernatant was pooled with the peptide supernatant, and subsequently dried using vacuum centrifugation. Peptides were re-suspended in 30 μ l of 5% formic acid in mass spectrometry grade water and subjected to mass spectrometry analysis.

DNA fiber assay

RKO *TP53*^{-/-} parental (WT) and *FANCI*-KO cells were plated onto 6-cm Plates 48 h before the experiment. Cells were sequentially labeled with two nucleotide analogs CldU (40 μ M) and IdU (100 μ M) for the indicated time. Aph was added to cells during the IdU pulse. After the IdU pulse, cells were treated with CSK100 buffer (100 mM NaCl, 10 mM MOPS, 3 mM MgCl₂ [pH 7.2], 300 mM sucrose, and 0.5% Triton X-100) for 10 min at room temperature (RT), then incubated with S1 nuclease buffer (30 mM sodium acetate [pH 4.6], 10 mM zinc acetate, 5% glycerol, and 50 mM NaCl) with or without 20 U/mL S1 nuclease (Invitrogen, 18001-016) for 30 min at 37 °C. The cells were then scraped in PBS + 0.1%BSA and centrifuged at 7,000 rpm for 5 min at 4 °C. PBS washes were done between each step. Cell pellets were resuspended at 500 cells/ μ L in PBS. The labeled cells were diluted with unlabeled at 1:2 ratio. 3 μ L cells were mixed with 9 μ L lysis buffer (200 mM Tris-HCl, pH 7.5, 50 mM EDTA and 0.5% SDS) on a clean slide, and dried at RT for 5 min. The slides were tilted, allowing the drops to flow down. The slides were air-dried at RT overnight. Fixation was done with 3:1 methanol/acetic acid for 1h at 4C, followed by denaturing with 2.5 M HCl for 1 h and neutralizing with 0.1 M Na₃B₄O₇ [pH 8], and three times washes with PBST. The slides were incubated in blocking buffer for 20 min and incubated with rat anti-BrdU (CldU: Abcam, ab6326, 1:200) in blocking buffer at 37°C for 1.5 h. After three washes with PBST, the slides were incubated with Alexa Fluor 488-donkey anti rat (Thermo Fisher, A-21208, 1:1000) for 45 min. After three times washes with PBST, the slides were incubated with mouse anti-BrdU (IdU: BD Biosciences, 347580, 1:50) for 1.5 h and then washed once with high-salt PBST (0.5 M NaCl) and twice with PBST. The slides were incubated with Alexa Fluor 555-donkey anti mouse (Thermo Fisher, A-11029, 1:1000) for 45 min. After three washes with PBST, the slides were mounted in ProLong Gold Antifade Mountant (Invitrogen, P36930). Images were acquired using the Zeiss LSM780 laser-scanning microscope (Oberkochen, Germany). The length of the CldU and IdU were measured by ImageJ software (NIH).

IncuCyte cell growth assay

For Aph dose-response assays in RKO *TP53*^{-/-} parental (WT) and *FANCI*-KO cells, 770 cells per well were seeded in 96-well plates and treated with sequential serial dilutions of Aph. After 6 days of treatment, the cell confluency was measured using an IncuCyte Live-Cell Analysis system (Sartorius). Confluence growth inhibition was calculated as the relative confluency compared to untreated cells. For proliferation assays of *sgDERA*- and *sgGNB1L*-expressing RKO *TP53*^{-/-} cells, 6000 cells per well were seeded in 24-well plates and treated with the indicated replication inhibitor or left untreated. The cell confluency was measured once 24 h post-seeding using an IncuCyte Live-Cell Analysis system. Growth curves were generated using confluency as the proxy for cell numbers.

dTAG-mediated protein degradation system

Two clonal 293T cell lines were generated by lentiviral transduction to introduce sg*GNB1L*-1 and the sgRNA-resistant *FKBP_{mut}*-*GNB1L* plasmid into the parental 293T cells. The dTAG^V-1 compound was added at 1 μ M for 1–24 h (short-term) or 1–6 days (long-term) to induce the degradation of the *FKBP_{mut}*-*GNB1L* protein.^{69,70}

HaloTag label-switch experiments

293T cells were transiently transfected with the Halo-ATR plasmid 24 h before the labeling experiments. To label newly synthesized Halo-ATR, cells were incubated with 10 μ M of the blocking agent 7-bromoheptanol⁸⁵ (Alfa Aesar, H54762), for 2 h, followed by two washes, and then incubated with 1 μ M TMR HaloTag ligand (Promega, G8252) for indicated time. To label pre-existing Halo-ATR, cells were incubated with 1 μ M TMR HaloTag ligand for 1 h, followed by two washes, and then incubated with 10 μ M blocking agent for the indicated time. Whole cell lysates were analyzed by SDS-PAGE and immunoblotting. TMR fluorescence signal was measured with a Typhoon FLA 9500 laser scanner (GE Healthcare). ImageJ (imagej.nih.gov) was used to quantify band intensities of TMR and α -actinin.

POPcode mutagenesis screen

The *GNB1L* open reading frame (ORF) was inserted into the pLVU/GFP lentiviral plasmid vector (Addgene, 24177) encoding a C-terminal GFP tag. The *GNB1L* coding sequence was subdivided into two regions, and variant libraries were generated via the oligonucleotide-directed mutagenesis method POPcode.^{72,73} Both *GNB1L* variant libraries were introduced into RKO *TP53*^{-/-} cells separately by lentiviral transduction. Cells were sorted for the GFP-positive population to select for *GNB1L*-GFP variant integration. Cells were then transduced with sg*GNB1L*-1 (Table S4) which targeted at an intron-exon junction site of the *GNB1L* gene. The γ -H2AX FACS screen was performed in cells with *GNB1L*-GFP variant library/sg*GNB1L*-1 in the presence of 150 μ M HU, as described previously in the “phenotypic CRISPR/Cas9 screen” section. Cells with the top 5% of γ -H2AX signal intensity were collected, and genomic DNA was extracted from both sorted and unsorted cells. The primer set (forward: 5' TCTGGCCGTTTTGGCTTTTT 3'; reverse: 5' GAACAGCTCCTCGCCCTTG 3') was used for PCR amplification of the inserted *GNB1L* ORF sequence. Variant frequencies in the pre- and post-selection libraries were assessed using TileSeq.^{72,73} Briefly, each ‘tile’ within the target locus was amplified with primers including Illumina sequencing adapters, followed by the addition of Illumina indices in a low-cycle PCR. Tiled libraries (including a wild type control) were sequenced by paired-end sequencing on an Illumina NextSeq 500 device using 300 cycle NextSeq 500/550 Mid Output v2.5 Kits, generating ~2M reads per tile. Sequencing data was processed as described previously.^{72,73} Briefly, libraries were demultiplexed with Illumina bcl2fastq and variant allele frequencies for each condition were calculated using the tileseq-package. Here, reads are aligned to a template sequence and mutations are called where there is agreement between both forward and reverse reads. Where read pairs disagreed, variants were treated as wild type. Fitness values were calculated using the tileseqMave pipeline⁸⁶ and scores were scaled based on the distribution of synonymous variants and the bottom 5th percentile of functional scores (in the absence of nonsense variants).

AlphaFold2 prediction of GNB1L-TELO2 interaction

Amino acid sequences corresponding to full-length human *GNB1L* and *TELO2*(460–640) were used as two separate chain inputs for the ColabFold implementation of AlphaFold2-multimer,^{87,88} using the following parameters: no templates, no amber relax, MMSegs2 MSA mode, AlphaFold2-multimer-v2 model type, 5 models, 3 recycles. The top-ranking model was used for further analysis. The predicted aligned error plot for the top ranking model is shown in Figure S10C. A plot displaying the mean interface predicted aligned error (PAE) is shown in Figure S10D. Mean interface PAE is defined as the average PAE value between the indicated *TELO2* residue and every *GNB1L* residue predicted to be within 9 Å. *TELO2* residues without any nearby *GNB1L* residues are assigned the maximum PAE value. Molecule display and analysis were performed in ChimeraX.⁸⁹

GO-Figure!

GO-Figure! analyses were done using the python script provided by Waterhouse Lab, using the top 80 GO terms sorted by adjusted p-value, as calculated by Enricher (<https://maayanlab.cloud/Enrichr/>). The GO-figure software clusters GO terms together at a similarity threshold of 0.5, using a weighted distance algorithm to describe proximity in the GO hierarchy. The figure represents similarity of GO term clusters based on their hierarchical proximity, with point color describing adjusted p-value of the representative term, and point size describing the number of GO terms within each cluster.

FoldX and rolling window analysis

$\Delta\Delta$ G scores were calculated using the BuildModel command of the FoldX software, following the methodology presented by ELELAB's mutateX algorithm (Figure S9B; Table S6). Each residue of the protein of interest was mutated to every other possible amino acid using the standard parameters of BuildModel.

The rolling window analysis plots (Figure S9B) take the rolling mean of each of three score types with a window size of five, therefore each position represents the mean of the given position along with the two scores before and after. The functional and $\Delta\Delta$ G scores were initially summarized for each position by taking the mean of all mutation scores for that residue, not including mutation to self or termination where it was provided. The conservation scores were calculated directly for each position with ConSurf (consurf.tau.ac.il/consurf_index.php).

QUANTIFICATION AND STATISTICAL ANALYSIS

All data presented are biological replicates unless otherwise stated. The statistical tests used, number of replicates, definition of error bars and center definitions are all defined within each figure or figure legend. Statistical tests performed in this study (Student's unpaired t-test) as well as nonlinear fitting of drug dose response curves were performed using Graphpad Prism 9. ns = $p > 0.05$, * = $p < 0.05$, ** = $p < 0.01$, *** = $p < 0.001$.